Università degli Studi di Padova

UNIVERSITY OF PADOVA

Department of Information Engineering
Master's Degree in ICT for Internet and Multimedia

Design and Implementation of UE Detection and Localization Algorithms Using Control Signals in Drone-Assisted 5G NR for Emergency Response

Supervisor
Prof. Marco Giordani

Co-supervisor

Master Candidate
Andrey Malikov

Academic Year
2024–2025

To my professors, family, parents, friends, and colleagues.

Abstract

In modern disaster response operations, the ability to locate users by their mobile phones without the need to be connected to terrestrial infrastructure has become a critical capability. This thesis investigates the use of Unmanned Aerial Vehicle (UAV) equipped with a 5G New Radio (NR) base station to detect and localize User Equipment (UE) based only on control signals. Using an OpenAirInterface-based testbed (OAIBox), we analyze the detection and localization potential of 5G NR uplink reference signals, such as the Physical Random Access Channel (PRACH) and the Sounding Reference Signal (SRS).

The proposed approach exploits the fact that even idle or disconnected UEs periodically transmit PRACH preambles during the initial access procedure, which can be passively received by the UAV. Different algorithms using Received Signal Strength (RSS) are developed to improve the reliability in Line-of-sight propagation (LoS) and Non-line-of-sight propagation (NLoS) conditions. The practical implementation involves configuring an OAIBox to capture and log physical-layer data in real time during UAV flights. The system design accounts for drone flight constraints such as power consumption, hovering time, and real-time signal processing limits. The proposed localization framework is validated through simulations, demonstrating the feasibility of infrastructure-independent UE detection in emergency or remote environments. An important contribution of this thesis is the design of an adaptive UAV flight strategy and signal-based UE localization algorithms. The flight strategy optimizes the drone trajectory for improved spatial coverage and measurement quality, while the proposed algorithms are tailored to operate reliably in both LoS and NLoS conditions. Simulations demonstrated that the proposed system can reliably detect user devices and achieve meter-level positioning accuracy under LoS conditions, while maintaining room-level accuracy in NLoS scenarios. This work lays the foundation for a fully autonomous drone-based localization system that can assist rescue teams in post-disaster scenarios, where conventional network access is unavailable.

Contents

Listing of figures

Listing of tables

Listing of acronyms

AoA Angle of Arrival

CPU Central Processing Unit

CSI-RS Channel State Information Reference Signal

CV Computer Vision

DMRS Demodulation Reference Signal

ESPRIT Estimation of Signal Parameters via Rotational Invariance Techniques

gNB Next Generation NodeB

IoT Internet of Things

JADE Joint Angle and Delay Estimation

LoS Line-of-sight propagation

MUSIC Multiple Signal Classification

NLoS Non-line-of-sight propagation

NR New Radio

NTN Non-terrestrial networks

PDSCH Physical Downlink Shared Channel

PRACH Physical Random Access Channel

PSS Primary Synchronization Signal

PTRS Phase Tracking Reference Signal

RAR Random-Access Response

RMSE Root-mean-square deviation

RSS Received Signal Strength

SDR Software-defined radio

SRS Sounding Reference Signal

SSB Synchronization Signal Block

SSS Secondary Synchronization Signal

ToA Time of Arrival

TRS Tracking Reference Signal

UAV Unmanned Aerial Vehicle

UE User Equipment

WLS Weighted least squares

1
Introduction

1.1 Problem and motivation

When natural disasters such as earthquakes, floods, or building collapses strike, terrestrial telecommunication infrastructures are often severely damaged or entirely disabled. This dramatically reduces the chances of successful rescue operations, especially during the first hours [1], when rapid intervention is crucial. In these contexts, mobile phones become the most reliable source of information: they are almost always carried by individuals and continue to emit control signals even in idle or disconnected states [2].

Traditional positioning solutions such as GPS, Wi-Fi, or cell-ID tracking are inadequate in such scenarios [3–5]. In fact, GPS signals, originating from satellites at over 20,000 km altitude, reach the surface with extremely low power and can be completely blocked by roofs, rubble, or underground environments. Wi-Fi and cellular network-based localization methods, on their side, rely on infrastructure that may no longer exist in disastered scenarios. Moreover, many classical smartphone geolocation methods implicitly require active user involvement, which cannot be assumed during emergencies: an app or system service must be allowed to share the position; the device must have enough battery and often data connectivity to upload it; privacy settings (e.g., disabled location or coarse-only mode) may block sharing; Wi-Fi fingerprinting/RTT needs a functioning, calibrated AP infrastructure; and operator-assisted cell-ID/timing methods presume a live radio access and core network. These assumptions often fail in disasters (people may be unconscious, devices off or locked, networks down). For this reason, there is a need for infrastructure-independent solutions that can detect and localize User Equipment (UE) based on their control signals alone, without relying on satellite visibility or ground network support.

1.2 Limits of current solutions

Recent research has highlighted Unmanned Aerial Vehicle (UAV)s and Non-terrestrial networks (NTN) as promising candidates for extending connectivity in disaster-struck areas [4–6]. UAVs equipped with software-defined 5G base stations can act as temporary gNodeBs and passively collect control signals from UEs. However, existing solutions face several limitations [2, 5, 7, 8]:

- **Infrastructure dependence:** many commercial and academic approaches assume at least partial terrestrial connectivity, e.g., cell-site simulators/IMSI-catchers that require network interaction for attachment/identification, Wi-Fi fingerprinting/RTT that presumes a functioning and calibrated AP infrastructure, and operator-assisted methods (cell-ID/OTDOA/TDOA) that rely on a live RAN and core [5, 7].
- **Signal restrictions:** downlink signals (e.g., SSB/CSI-RS/TRS) are transmitted by the gNB and cannot be directly exploited at the receiver side for UE localization from a drone, while some of the uplink ones require the UE to be already `RRC_CONNECTED` and configured, whereas PRACH is available only when the UE attempts initial access [2].
- **Processing constraints:** a UAV must trade battery, payload mass, and onboard compute. With a multi-kg SDR+gNB payload, effective flight time shrinks to minutes, so the mission budget is dominated by transits and short hovers. In practice this forces (i) coarse–to–fine scanning (20–40 coarse points + 1–4 refined zones) rather than uniform dense coverage; (ii) short dwell per point ($\approx$3–5 s) to average a handful of uplink RSS/PRACH snapshots; (iii) lightweight, single-pass signal processing on board (synchronization, PRACH detection, RSS logging), with heavier routines (e.g., full multilateration under model checks) deferred or pruned. These constraints directly cap algorithmic complexity, sampling density, and trajectory length, and motivate the adaptive Cold–Warm–Hot strategy used later.
- **Non-line-of-sight propagation (NLoS) propagation:** obstacles such as walls, reinforced concrete, coated glass, or debris add strong attenuation and excess delay that systematically corrupt Received Signal Strength (RSS)-based distance estimates. As a result, range-based multilateration becomes unstable: several anchors "see" a much weaker and delayed signal, the geometry turns ill-conditioned, and the solution drifts far from the true position (large bias/variance). In practice this means (i) range solvers should be used only in predominantly LoS-like scenes; (ii) in mixed visibility it is safer to rely on relative RSS peaks (heatmaps) rather than converting RSS to ranges; and (iii) mitigation requires either explicit obstacle awareness (to compensate penetration losses) or trajectory/altitude adjustments to reduce blockage.
- **Lack of open reproducible platforms:** commercial systems like Lifeseeker™ [9] demonstrate feasibility but remain closed and proprietary, with limited academic transparency.

Thus, there remains a gap in passive UE localization under conditions of complete infrastructure destruction, using only uplink cellular control signals such as Physical Random Access Channel (PRACH).

1.3 Contributions of this thesis

This thesis addresses the gap by proposing a UAV-assisted 5G New Radio (NR) localization system built with help of an OpenAirInterface-based experimental platform (OAIBox) [10]. The main contributions are:

1. **Characterization of control signals for localization** - protocol- and signal-level analysis of 5G NR uplink references, with an emphasis on PRACH as the primary passive detection signal for idle/inactive UEs.

2. **Design of an adaptive UAV flight strategy** - introduction of a multi-stage "Cold–Warm–Hot" exploration approach for area scanning and UE discovery/localization under strict flight-time and payload constraints, optimized to balance spatial coverage, measurement density, and battery limits.

3. **Development of RSS-based localization algorithms** - implementation of two complementary approaches:

   - a heatmap-based estimator that relies on relative RSS patterns and local peak selection, robust to mixed visibility (LoS/NLoS) and suited for room-level accuracy;
   - RSS-to-range multilateration solved via WLS, enabled only under LoS-like conditions according to a decision rule and calibrated on site (reference power/path-loss), targeting meter-level coordinates.

4. **NLoS-aware corrections** - integration of material penetration losses to moderate localization errors in NLoS environments, including experimental evaluation of material-aware corrections.

5. **Validation on real hardware** - practical tests with OAIBox and in-lab simulations, demonstrating reliable passive UE detection via PRACH, meter-level accuracy in LoS with WLS, and stable room-level estimates in mixed visibility via heatmaps; the flight-time budget supports coarse-to-fine scanning (36 coarse points and up to 1-4 refined zones) with 3-5 s dwell per point.

1.4 Thesis structure

The thesis is organized as follows:

- Chapter 2: background on emergency communication, UAV-assisted NTNs, and 5G NR signaling relevant to detection and localization; research gap.

- Chapter 3: design of the adaptive flight algorithm, including the Cold–Warm–Hot model, time/power analysis, and NLoS-aware extensions.

- Chapter 4: RSS-based localization algorithms - heatmap methods, Weighted least squares (WLS) multilateration, accuracy metrics, and obstacle-aware corrections.
- Chapter 5: results of extensive simulations under different configurations.
- Chapter 6: conclusions, limitations, and directions for future research.

2

Introduction on the topic and literature review

2.1 Emergency communication and the role of 5G in disaster situations

Traditional telecommunication infrastructure is often damaged or completely disabled when disasters like earthquakes, floods, buildings' collapses or military attacks occur. This dramatically reduces the chances of success for rescue operations, especially within the first hours, when readiness in response is critical. In such situations, the top priority is represented by the rapid detection and localization of civilians in extreme need. In general, the mobile phone is a device that people usually carry on with themselves during everyday tasks. Even in idle mode, without active user participation, smartphones continue to periodically transmit control signals into the air, trying to register in an available network. These signals can be used as passive beacons to indicate the presence of a user in a particular location although, when it comes to use existing positioning systems such as GPS, Wi-Fi-based localization or cell-ID tracking, these are often unsuitable or extremely inaccurate if the infrastructure is out of service. For example the Global Positioning System (GPS) is a collection of satellite constellations used for global navigation, that offers a well-known method of geopositioning on modern mobile devices. However, despite its popularity, this technology has a few significant limitations, especially in emergency scenarios.

First, the GPS signal is transmitted by satellites from an altitude of over 20,000 kilometers and reaches the Earth's surface with an extremely low power level. Because of this, even thin barriers such as roofs, concrete slabs, walls or rubble can completely block signal reception. In other cases, like indoor, underground or under debris, geolocalization can become impossible [3]. In addition, the phenomenon of multipath distortion can occur in dense urban environments or when there is a limited view of the sky, in any case, GPS is notoriously inaccurate, and may not be the ideal candidate in this emergency scenario.

Secondly, it is important to consider that the geopositioning signal receiver inside a phone is a purely passive component that receives signals from satellites and locally computes coordinates. No information is automatically transmitted outwards. For the geo-position to become available externally (e.g. to the emergency services), these following requirements shall be met:

- a running application or system service that transmits coordinates;
- sufficient battery power and smartphone activity.

In emergency situations, these preliminary conditions are often not met. For instance, the network may be destroyed, data transmission may be unavailable, the user may be unconscious, or the device may be locked. Therefore, even if the coordinates may have been determined, they may not be obtained by an external system from the outside. Since classical localization approaches assume active user participation and availability of working infrastructure, this makes classical geopositioning technologies unsuitable for passive user-localization tasks in case of out-of-order infrastructure. Moreover, the pre-existing infrastructure might be overloaded or slowed down in terms of readiness, especially during emergencies. This raises the need for an infrastructure-independent solution that can detect and localize smartphones by catching their control signals, without user involvement and without network availability.

2.2 Non-Terrestrial Networks and UAV-Assisted 5G Systems

In recent years, the concept of NTN has been widely developed as a promising goal for extending mobile network coverage in hard-to-reach, remote or destroyed regions. According to 3GPP definition [6], NTN covers any telecommunication systems that utilizes platforms that are not on the Earth's surface: satellites, stratostats, aerostats and unmanned aerial vehicles (UAVs).

The most interesting applications for emergency communications are low-altitude mobile platforms such as drones with embedded 5G base stations. Thanks to their ability to quickly reach disaster areas, UAVs can provide temporary wireless coverage whereas terrestrial infrastructure is unavailable or failing [4, 11, 12].

NTN advantages in disaster scenarios are:

- Rapid deployment: a drone with a base station can be launched towards a disaster area without the need for on-site transportation and equipment installation.
- Mobility and flexibility: the platform can change position in real time for optimal coverage, area scanning and adaptation to relief.
- Infrastructure independence: no need to connect to the transportation network, optical core or power supply, basically the system operates autonomously on battery power.
- Remote and safe operation: UAVs can be piloted and supervised from a distance, allowing human operators to remain outside hazardous zones while maintaining communications support.

- Support for 5G NR technology: existing Software-defined radio (SDR) platforms allow the entire 5G NR stack to be implemented in a mobile configuration using frameworks like OpenAirInterface.

Current research highlights the potential of NTNs to overcome the limitations of traditional communication systems, especially in remote and infrastructurally deprived regions. The work of Giordani and Zorzi [4] emphasizes the challenges and prospects of using NTNs in the 6G era, including their role in providing reliable communication in the absence of terrestrial infrastructure. Similarly, a recent study by Wang et al. [13] considers the use of UAVs, high-altitude platforms (HAP) and low Earth orbit (LEO) satellites to support Internet of Things (IoT) within multi-layer NTN architectures. In parallel, the trade-off between capacity, coverage, and power on UAV platforms has also been studied in mmWave settings, where beamforming design critically impacts feasibility [14]. While these works demonstrate the potential of such solutions for global coverage, they do not focus on passive localization of users via uplink control signals, which is the subject of this thesis. Beyond coverage-oriented NTN studies, prior UAV/SDR localization efforts show feasibility but rely on active or controlled transmissions, not on passive discovery of idle UEs via standard NR control signals (e.g., PRACH) [15, 16]. Moreover open and reproducible airborne systems for passive PRACH-based UE detection remain scarce; commercial SAR tools (e.g., Lifeseeker™) demonstrate viability but are closed-source [9].

UAV as an element of NTN: architecture and challenges

Within the NTN ecosystem, drones can act as temporary gNodeBs transmitting and receiving signals. An architecture of such a node includes PC with a 5G stack installed, software-defined radio module [10, 15], and battery. An example of such a system is the OAIBox [10], designed for mobile 5G experiments. It combines a fully functional 5G stack with SDR and can receive control signals from the UE in the uplink channel, even in the absence of an uplink connection from the user side. Despite the big potential, the practical realization of UAV-NTN systems encounters some challenges:

- Synchronization difficulties: for accurate channel impulse response estimation, a stable time base and accurate positioning of the drone are required.

- Power and Central Processing Unit (CPU) limitations: autonomous flight time and local processing capabilities on the drone are limited, requiring computational optimization.

- Quality of reception in challenging environments: reflections, multipath, and variable environments can distort the received signal and make it difficult to extract metrics.

Nevertheless, with proper design, such platforms can passively detect smartphones from their control signals, measure signal strength, delay, and angle of arrival, and use this data to estimate the position of a UE in a disaster area.

2.3 Overview of 5G NR signaling for detection and localization

To implement passive user localization in fifth-generation networks, it is necessary to deeply understand the architecture of signaling procedures in 5G NR. Unlike previous generations [17], 5G NR offers an extended set of control and reference signals in both uplink and downlink directions. These signals play a key role in link initialization, synchronization, channel quality measurement and resource management. Some of them can be used as “signals of opportunity” - sources of information about the presence and location of UE, even without its active participation in the communication. Among the numerous 5G NR control signals, some are used in the initial access phase, while others are used when the UE is already connected. The division and usage of these signals are as follows:

Review of the signals for establishing connection

In the uplink direction, for the initial establishment of connection, PRACH plays a key role. It is employed by UEs to initiate network access procedures, including initial attachment, handovers, and re-establishment of lost connections. During this process, the UE selects randomly one contention-based PRACH format, chooses one available preamble, which is subsequently detected by the Next Generation NodeB (gNB). The gNB sends back (MSG2) to the UE, on the Physical Downlink Shared Channel (PDSCH), a Random-Access Response (RAR), enabling synchronization and resource allocation [18]. The PRACH signal is particularly valuable in emergency contexts, because it can be transmitted by UEs even when they are not connected to the network. When the presence of a base station is detected, like a drone-based gNB, idle or disconnected UEs autonomously initiate PRACH procedures to re-establish connectivity. When using PRACH, we have a known sequence: 5G NR uses Zadoff-Chu sequences that have good autocorrelation properties [19]. This can be used to accurately determine when the signals are transmitted, as well as the Time of Arrival (ToA). Hence PRACH is good for ToA estimation, especially when the bandwidth is wide enough. By passively receiving these transmissions, the gNB can also measure the received signal power to infer relative proximity. As PRACH operation does not require the UE to be in a connected state, it is highly suitable for detecting devices under emergency or idle conditions.

In the downlink, several control and synchronization signals are used to enable UE discovery and facilitate network attachment. The Primary Synchronization Signal (PSS) and Secondary Synchronization Signal (SSS) are integral components of the Synchronization Signal Block (SSB). These signals are periodically broadcast by the gNB, often with directional beam sweeping to cover different spatial sectors. The PSS is used for cell search and initial access; it is the first signal that a device searches for when it first accesses the network. The SSS acquired after the PSS supplies additional synchronization data, determines the Physical Cell Id (PCI) of the detected cell. Therefore, these signals are ones of the few 5G NR “always-on” signals. These signals are essential for idle or powered-on UEs to detect and synchronize with a cell and initiate access procedures via PRACH. However, as downlink-only signals, PSS and SSS cannot be used directly for localization.

Review of the signals in connected state

For UEs that are already in the `RRC_CONNECTED` state, the Sounding Reference Signal (SRS) is very important. The SRS is transmitted by the UE upon request by the gNB. As proposed by the 5G standard, the SRS is used for uplink positioning. The transmitted SRS sequence is generated and mapped into the allocated subcarriers [20]. The gNB sends an RRC message to the UE containing the SRS configuration parameters. These parameters include frequency, time, duration, bandwidth, and type (periodic, on demand, etc.). This configuration allows the gNB to estimate channel quality in the time, frequency, and spatial domains. In the context of localization, the SRS is especially beneficial due to its strictly defined shape and frequency-time structure, which simplifies channel estimation and ToA/Angle of Arrival (AoA) determination. Three conventional Angle-of-Arrival algorithms have been already studied and implemented: Multiple Signal Classification (MUSIC) [21], Estimation of Signal Parameters via Rotational Invariance Techniques (ESPRIT) [22] and Joint Angle and Delay Estimation (JADE) ESPRIT [23]. Additionally, the SRS can be used to estimate ToA (under the condition of high-precision synchronization between UE, gNB and received signal power since the main task of uplink SRS is that the base station measures the power of the incoming signal to control uplink link budget, adjust uplink power control, assess channel quality. However, the transmission of SRS is contingent on the UE being in connected mode and having been configured by the gNB to transmit the signal.

Another signal of interest is the Demodulation Reference Signal (DMRS), which is in both downlink (PDCCH, PDSCH, PBCH) and uplink (PUCCH and PUSCH). In the uplink, DMRS assists the gNB in demodulating user data and performing channel estimation. However, DMRS is only transmitted together with the data, it is only inserted into the resource if the UE is already transmitting something (e.g. UL data or CSI). Therefore, in an emergency, when there is no active transmission, DMRS does not appear at all. Moreover, unlike PRACH or SRS, DMRS does not have a fixed temporal structure, it shifts relative to the beginning of the slot depending on the configuration. Therefore, a DMRS-based ToA can only be determined if all transmission parameters are known, including schedule, slot start, symbol. For the sake of a simplified and effective operation, this approach is just too complex for our purposes. Another technique considered is the Phase Tracking Reference Signal (PTRS), that works in combination with DMRS and exists in both downlink and uplink directions. It is used for fine granularity of the phase in time. Like DMRS, PTRS is not a standalone signal - it is inserted into the transmission only when data is scheduled. Therefore, due to its dependency on data transmission, lack of standalone scheduling and unsuitability for channel estimation or spatial resolution, PTRS is not a viable candidate for user localization.

Channel State Information Reference Signal (CSI-RS) used by the UE to derive information about the downlink channel (channel estimation and sounding) over which it is sent. It can be detected by every UE (also in idle mode, or neighbors in adjacent cells) to perform channel estimation. While CSI-RS has a well-defined structure and supports high-resolution channel measurements, it is inherently unsuitable for user detection and localization from a drone-based platform, because it is transmitted from the gNB and requires the UE to receive and process the signal. As a result, the gNB cannot directly measure signal characteristics from the user equipment. While CSI-RS itself does not provide localization data, it may indirectly contribute to localization by prompting the UE to transmit CSI-RS feedback or engage in other uplink procedures that include locatable signals, but uplink-based signals such as PRACH or SRS are better suited for this purpose. The Tracking Reference Signal (TRS), also transmitted in the downlink, is intended to refine time and frequency synchronization following initial access. TRS is typically sent less frequently than CSI-RS, particularly in Frequency Range 1 (FR1), and is applicable only when the UE is in connected mode. Like CSI-RS, TRS does not directly provide localization capabilities.

Overall, the most critical signals for UE detection in disaster-response scenarios are the PRACH and SRS. PRACH is ideal for detecting idle/disconnected UEs due to its contention-based access mechanism using the PRACH preambles (Fig. 2.1). SRS is the best option for connected UEs, offering structured sequences for high-accuracy ToA and AoA. However, due to the requirements regarding pre-configuration from the gNB and connection availability, SRS is less versatile in emergency situations. Downlink signals (PSS/SSS, CSI-RS, TRS) are unsuitable for direct localization, while DMRS/PTRS depend on active data transmission, making them unreliable in emergencies. Thus, PRACH is the primary source of signals for passive localization in a collapsed infrastructure, while SRS can be used as an additional tool for position refinement, especially after connection establishment.

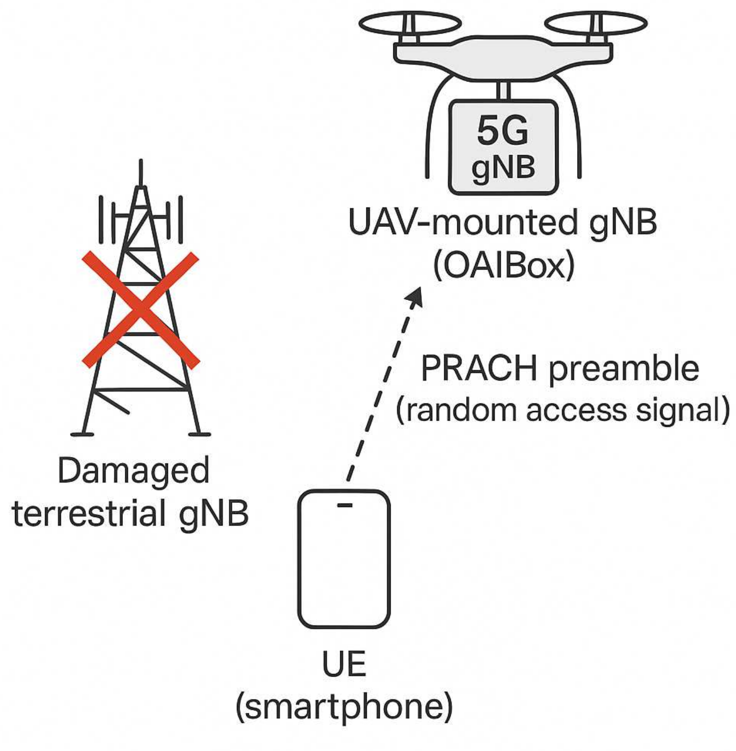

Figure 2.1: Example disaster-recovery scenario: a UAV-mounted gNB (OAIBox) captures PRACH preambles from smartphones in the absence of terrestrial infrastructure.

2.4 Review of existing approaches and research gap

In recent years, the growing need for resilient and autonomous user localization systems in disaster-affected areas has stimulated extensive research at the intersection of UAV platforms, software-defined radios (SDRs), and 5G/6G signal processing. Several promising directions have appeared, highlighting both the potential and current limitations of the state-of-the-art. Current research demonstrates the high potential of using drones for positioning and monitoring tasks. For example, Yi Li et al. [16] proposed a system for determining the position of the UAV itself based on CSI analysis and estimation of signal arrival angles. Despite the high accuracy achieved in a controlled environment of about 2 meters, these solutions focus on the positioning of the drones themselves rather than user equipment. Thus, there remains a gap in the field of passive localization of UEs in non-networked environments, especially using uplink control signals. Simultaneously, several works have demonstrated the feasibility of UAV-based localization using SDR platforms. Codău et al. [15] proposed an airborne architecture using a uniform circular antenna array (UCA) and the MUSIC algorithm on board the drone, providing accurate AoA estimation up to 2.5 km. While the results confirm high spatial accuracy, the system targets active signals and controlled conditions rather than idle user scenarios [24]. Recent studies confirm the increased interest in RSS localization, especially in the context of limited availability of accurate information about transmitters and environment. For example, the work of Yi Li et al. [25] demonstrates the feasibility of highly accurate localization even in the face of uncertain values of transmitter power, signal loss exponent (PLE), and anchor node positions. The authors propose a cooperative strategy (CTUP) capable of estimating all unknown parameters simultaneously using a mixture of SDP-SOCP techniques. Such an approach confirms the relevance of using RSS for positioning tasks in wireless networks under limited information. Additionally, the energy consumption constraints of UAV edge computing in NTN scenarios have been recently analyzed [26], which directly relates to the endurance limitations of drone-assisted platforms. Despite the limited number of open publications, there are several commercial systems demonstrating a growing interest in the concept of autonomous localization of users based on their cellphones' signals. One example is given by the Lifeseeker system [9], already used in rescue operations in Europe and the USA. It allows to detect and localize smartphones with high accuracy, including scenarios with complete network absence, by activating the phone in IMSI catch mode (2G/3G/4G) or using broadcast interaction. However, the details of its implementation and algorithms remain undisclosed. Despite the development of highly accurate and commercially successful solutions, there is a lack of open, reproducible and passive platforms capable of detecting user devices in idle state relying only on uplink control signals. The main goal of this thesis is to show that the implementation of such devices is not only feasible and accessible, but also crucial for such applications, in addition to being a strong improvement on current localization technologies.

Research gap

Currently, there are virtually no solutions that can:

- passively detect UEs without user involvement.

- operate in the complete absence of network infrastructure.
- use standard 5G NR control signals (e.g. PRACH) transmitted regardless of the established connection.
- perform on-the-fly localization using drones with gNB installed.

There is an opportunity to develop a new class of systems based on UAV-mounted 5G gNBs capable of receiving uplink control signals from UEs, extracting signal parameters and performing localization in real-time. This study aims to address the mentioned gap. The system under development combines:

- UAV with SDR infrastructure (OAIBox);
- overflight and signal scanning algorithms;
- localization techniques based on passively received RSS.

Such approaches are considered key in the context of 6G and emergency communication systems development. For example, the review by Alnoman et al. [27] surveys AI- and 6G-enabled user localization for emergencies, emphasizing robust, infrastructure-lean techniques when GNSS and cellular networks are impaired. The authors highlight signals-of-opportunity and ML-enhanced positioning as promising directions, which supports the relevance of our chosen approach.

3 Flying algorithm design for adaptive RSS exploration

This chapter introduces an adaptive drone-based flying algorithm. The algorithm is designed specifically for recording spatially distributed RSS values for subsequent localization of UE. The key element of proposed method is a flight strategy based on the “Cold–Warm–Hot” principle, meaning that the drone dynamically adapts the trajectory using prior signal measurements.

3.1 ”Cold–Warm–Hot” architecture

The flight strategy can be formally structured as a three-stage adaptive architecture, commonly referred to as the “Cold–Warm–Hot” model. It is known that multi-stage adaptive scanning methods significantly improve localization efficiency by dynamically allocating resources based on measurement results. We perform a 5-meter additional exploration and take the peak of the refined heat map.

Cold phase — rough measurement: the drone starts to fly above the region of interest, of size 100×100 m, using a “Lawnmower Pattern” (see Figure 3.1) with a step of 20 m between the stops, making RSS measurements. The goal here is to highlight a common signal fluctuation and to define potentially interesting areas.

Warm phase — identifying candidate cells: based on the results of the first phase, the regions are highlighted where RSS is higher than a predefined threshold. To increase robustness to a variable signal environment, the warm cells detection threshold is determined adaptively, based on the average signal strength measured during the coarse scan. This approach ensures that areas with relatively strong signal are selected without using hard-coded thresholds. Adaptive thresholding methods, based on the relative difference from mean RSS values, have shown increased

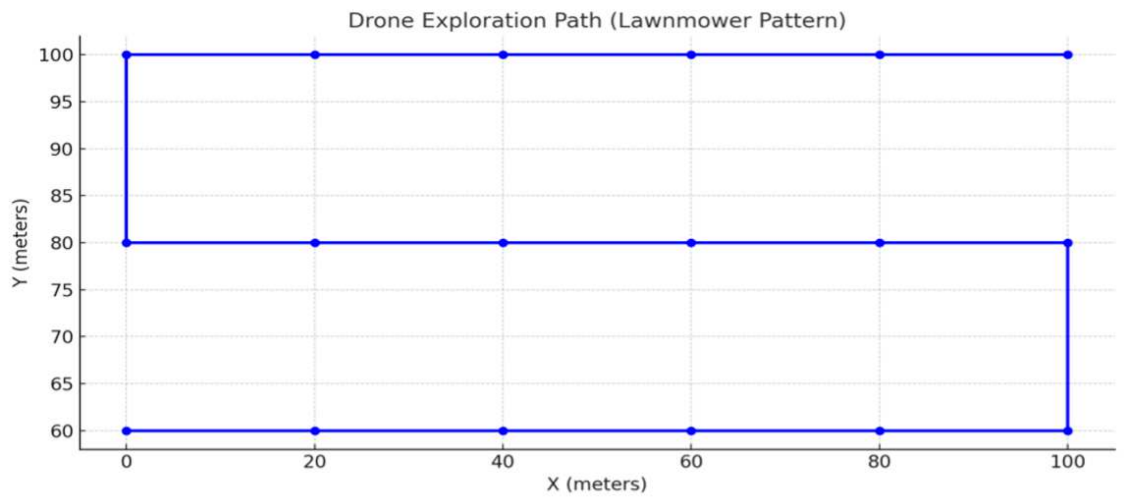

Figure 3.1: Planned drone path using lawnmower coverage pattern.

robustness in varying environmental conditions compared to fixed-threshold techniques [28].

Let the disaster area be $\mathcal{A} \subset \mathbb{R}^2$, discretized by a coarse grid $G = \{p_1, \ldots, p_J\}$, where each p_i denotes a UAV measurement position. We define the grid spacing as Δ (e.g., $\Delta = 20\,\mathrm{m}$ in the coarse scan). A grid cell C_i is the square region of side Δ centered at p_i. By convention, C_i inherits the measurement value at its center. At every grid point $p_i \in G$, the UAV collects K short RSS snapshots and stores their average value $\overline{R}(p_i)$. The global background level is then defined as

$$\overline{R}_{\text{global}} = \frac{1}{J}\sum_{i=1}^{J} \overline{R}(p_i), \tag{3.1}$$

while the statistical variability of the measurements is captured by the sample standard deviation s computed over the set $\{\overline{R}(p_i)\}_{i=1}^{J}$.

Warm-cell rule. A grid cell C_i is classified as warm if its average RSS significantly exceeds the background level:

$$\overline{R}(p_i) > \overline{R}_{\text{global}} + \Delta, \tag{3.2}$$

where Δ is a detection threshold chosen to suppress false positives due to shadowing noise. Specifically, a measurement point in the grid is classified as a warm cell if its RSS value exceeds the average RSS value by at least 5 dB. This threshold was chosen because shadowing variations in FR1 are typically on the order of 4–8 dB (3GPP TR 38.901 [8]), and a margin of 5 dB corresponds to approximately two standard deviations ($\approx 95\%$ confidence). Hence, exceeding this margin indicates a genuinely stronger signal region rather than random fading fluctuations. Warm cells define a refined set of targets $F \subset \mathcal{A}$. We rescan F using a denser grid (5 m step size), concentrating flight time where the signal is promising and increasing map resolution at limited energy cost.

Hot phase — detailed measurement: In each of the warm cells a local high-resolution scan is performed using the pattern of more detailed "Lawnmower Pattern" with the step of 5 m between the stops (see Fig. 3.4.). This refines the RSS profile and improves the accuracy of subsequent localization This structure allows the drone to spend more resources on the potentially important areas, save energy, and increase the resolution of the map.

3.2 Objectives and constraints

The main objective of the flight pattern is the construction of a high-precision RSS map within the zone of interest with minimum measurement redundancy and maximum localization accuracy. The following limitations are considered:

- Coverage performance: the whole area (e.g., a 100×100 m region) must be covered with adequate spatial resolution.

- UAV altitude: In simulations, the UAV altitude is varied within the range 30–300 m. This range is consistent with the deployment scenarios considered in 3GPP TR 38.811 for low-altitude platforms within NTN, where UAVs typically operate from tens to several hundreds of meters above ground level. For simplicity, distances are computed in the 2D ground plane, while the vertical offset is treated as a known correction. The resulting 2D–3D distance mismatch introduces a deterministic error ($\approx$2 m at 30 m horizontal separation, <0.5 m at 100 m), which is on the same order as the shadowing variance ($\sigma \approx 2$ dB) and much smaller than NLoS effects. This offset can be subtracted from the final Root-mean-square deviation (RMSE), ensuring that the reported positioning accuracy is not biased by the 2D approximation.

- Measurement quality: measurements must be accurate and gathered with sufficient density to enable reliable localization. To obtain reliable measurements at each coordinate point,, the UAV hovers and collects at least three RSS samples which are then averaged. In our setup, the OAIBOX dashboard exposes UE PHY KPIs as real-time plots and time-stamped logs; the logging frequency is approximately 1 Hz (one record per second), limited by the dashboard/export layer. Thus, hovering for 3–5 s yields 3–5 samples per point, which mitigates short-term fading and RSS jitter through temporal averaging.

- Adaptivity: the algorithm must react to changes in signal measurements and focus on zones with the highest probability of finding the UE.

- Power and time constraints: the drone's limited battery capacity imposes strict constraints on flight duration and necessitates efficient trajectory planning. In this work, we assume the use of the Drone X4-1000 Pro RTK (already available in the lab). The OAI experimental payload (including OAIBox and associated equipment) is approximately 9 kg. According to the manufacturer's specifications [29], the X4-1000 Pro RTK can carry payloads up to 10 kg, which is suitable for our purposes.

The flight endurance is estimated using the standard multirotor hover-power scaling, see Equation (3.3):

$$T(P) \;=\; T_0 \left(\frac{W_0}{W_0 + P}\right)^{3/2}, \tag{3.3}$$

where $T(P)$ is the expected hover time (min) with payload P (kg), T_0 is the hover time with no payload, and W_0 is the take-off mass without payload (kg); the loaded mass is $W = W_0 + P$. Using the no-payload reference from the drone specifications, [29] $T_0 = 50$ min and $W_0 \approx 11$ kg, with the experimental payload $P \approx 9$ kg (thus $W = 20$ kg), we obtain:

$$T(9\,\mathrm{kg}) \;=\; 50 \left(\frac{11}{20}\right)^{3/2} \;\approx\; 50 \times 0.4089 \;\approx\; 20.4\ \mathrm{min}.$$

In addition to the hover–power scaling in (3.1), we must budget the time to reach and leave the target area. Let D_{site} be the one–way distance from the takeoff point to the first grid location and v the cruise speed. The ferry time is

$$T_{\mathrm{ferry}} \;=\; \frac{2\,D_{\mathrm{site}}}{v}\,.$$

To ensure mission safety, a fraction α of the total time is reserved for return-to-launch (RTL) and contingencies; we set $\alpha = 0.30$:

$$T_{\mathrm{RTL}} = \alpha\,T, \qquad T_{\mathrm{eff}} \;=\; T - T_{\mathrm{RTL}} - T_{\mathrm{ferry}} \;=\; (1-\alpha)\,T \;-\; T_{\mathrm{ferry}}\,,$$

where T_{eff} is the effective on-site time available for measurements and short transits between grid points.

We adopt a conservative cruise speed of $v = 3\,\mathrm{m/s}$, consistent with survey/inspection practice (2–8 m/s) [5]. The average transit time between coarse-grid points at 20 m spacing is:

$$t_{\mathrm{transit}} \;=\; \frac{20\,\mathrm{m}}{v} \;\approx\; 6.7\,\mathrm{s}\ \text{for}\ v = 3\,\mathrm{m/s}.$$

Assuming 4 s of hovering per point to record at least three measurements (at ≈ 1 Hz) and 7 s of transit per move, each coarse grid point requires ≈ 11 s. For a 100×100 m area with 20 m resolution (a 6×6 grid including the boundary, i.e., 36 points), the total time for the coarse scan is:

$$T_{\mathrm{coarse}} \;=\; 36 \times 4 \;+\; 35 \times 7 \;=\; 389\ \mathrm{s}.$$

This leaves approximately 471 s of effective flight time for adaptive high-resolution refinement in warm cells, enabling a two-stage strategy with both wide-area coverage and localized precision. For the refinement step, we assume a step size of 5 m in a localized 4×4 grid within a warm cell

(16 points). With 4 s hovering and 2 s moving per point, the total time required is:

$$T_{\text{warm-cell}} = 16 \times 4 + 15 \times 2 = 94 \text{ s}.$$

Hence, within the remaining 471 s after the coarse scan, the UAV can survey up to four warm cells at high resolution before the RTL deadline. These principles define the overflight architecture and justify the use of a multi-stage scanning strategy. In the numerical example below we fix the coarse grid spacing to 20 m and the refinement spacing to 5 m (hover dwell 4 s; cruise speed 3 m/s). Other choices scale the timings accordingly.

3.3 Scenario simulation and visualization

For demonstration of the proposed algorithm let us consider scenario where UE is located at the point (65,40) (Fig. 3.2). Drone is performing the coarse scanning of the grid with the 20m step. In one of the cells close to the real position of the UE a high RSS value is registered. Thereofore, based on the warm-cell rule, a refined (more detailed) scanning is performed in that cell (warm phase), using a 5 m step grid. Using this approach, we can measure the whole region of interest estimating the precise position of the UE, and verify whether this elevated value was not caused by random signal fluctuation. A numerical simulation in Python was performed to verify the effectiveness of the overflight algorithm. A UE is assumed to be located at an unknown position inside a 100×100 m zone. The drone overflights a coarse grid of 6×6 points with 20 m spacing, collecting RSS measurements at each point. The signal is modeled by a logarithmic attenuation model with lognormal shadowing (σ=2 dB), which corresponds to an open zone scenario:

$$\text{RSS}(d) = \text{RSS}_0 - 10\, n \cdot \log_{10}\left(\frac{d}{d_0}\right) + X_\sigma. \tag{3.4}$$

This is the standard log-distance path-loss model with lognormal shadowing [7, 8, 30].

where $d_0 = 1\,\text{m}$; X_σ is the shadowing term modeled as a zero-mean Gaussian random variable, i.e., $X_\sigma \sim \mathcal{N}(0, \sigma^2)$, with $\sigma = 2\,\text{dB}$ [8, 30]; $n = 2$ is the path-loss exponent; and RSS_0 is the reference received signal level (in dBm) at the reference distance $d_0 = 1\,\text{m}$ under LoS conditions and fixed transmitter settings. RSS_0 was calibrated on site in the lab. In practice, we placed the UE and the OAIBox gNB at d_0, collected K snapshots ($K \approx 50$–100), and took their average as RSS_0. We measured $RSS_0 = -75\,\text{dBm}$. Since RSS-to-range conversion relies on RSS_0, any calibration bias directly rescales the inferred distances and degrades WLS performance; thus we perform this calibration *prior to the fast path*.

Notice that warm cells are detected when the local average RSS exceeds the global average by $\Delta = 5\,\text{dB}$. Since $\Delta \approx 2.5\sigma$ in our model ($\sigma = 2\,\text{dB}$), this corresponds to a $\approx 99\%$ confidence threshold that the observed difference is not due to shadow-fading noise.

After data collection, the average RSS at each point is calculated (Fig. 3.2). Based on these values, the cell with the maximum signal strength is determined, which is identified as the "warm cell". A refining grid of 5 × 5 points with a step of 5 m is formed around it, where the drone performs new measurements (Fig. 3.3). Increasing the sampling density allows us to more accurately localize the signal maximum while avoiding unnecessary coverage of the entire area.

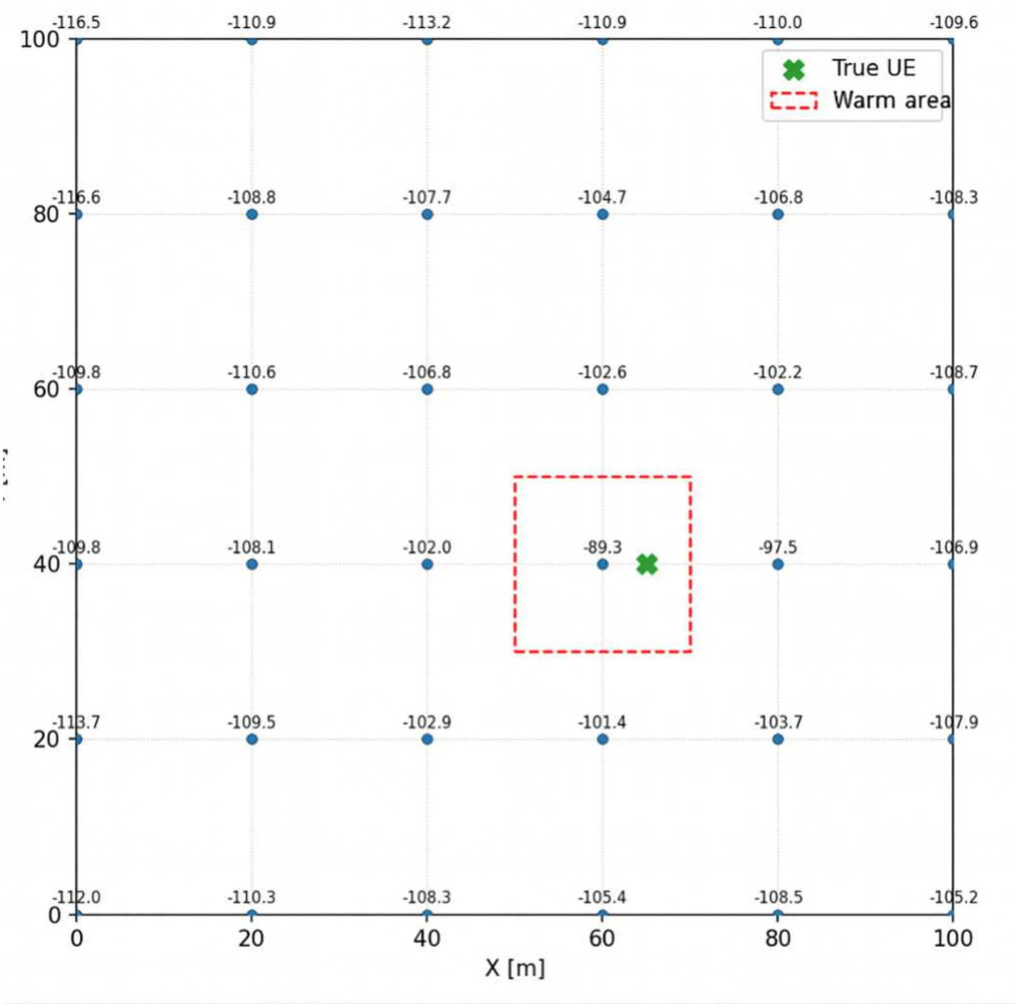

Figure 3.2: The average RSS at each point.

The efficiency of the proposed algorithm is demonstrated with help of two heat maps:

1. RSS heatmap obtained during coarse scanning: it depicts the spatial distribution of RSS measurments on the initial grid, showing the common gradient of the signal and highlights the warm cells (see Figure 3.5). The coarse RSS map is visualized by interpolating the 36 measured samples (20 m resolution) onto a 1 m raster using `griddata` (cubic with linear/nearest fallbacks). The color field therefore represents an interpolated RSS surface rather than additional measurements. Interpolation is used purely for visualization and for locating the local warm region; quantitative metrics still rely on the original samples (or on

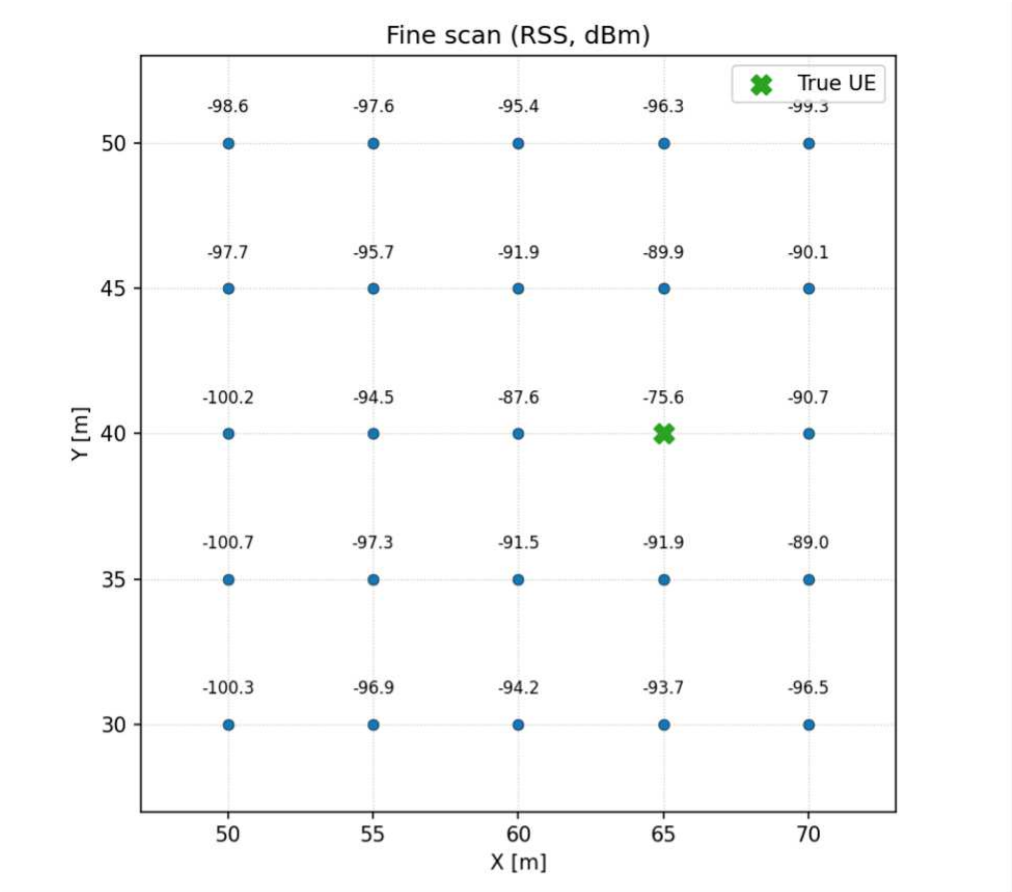

Figure 3.3: The average RSS of the refinement scan.

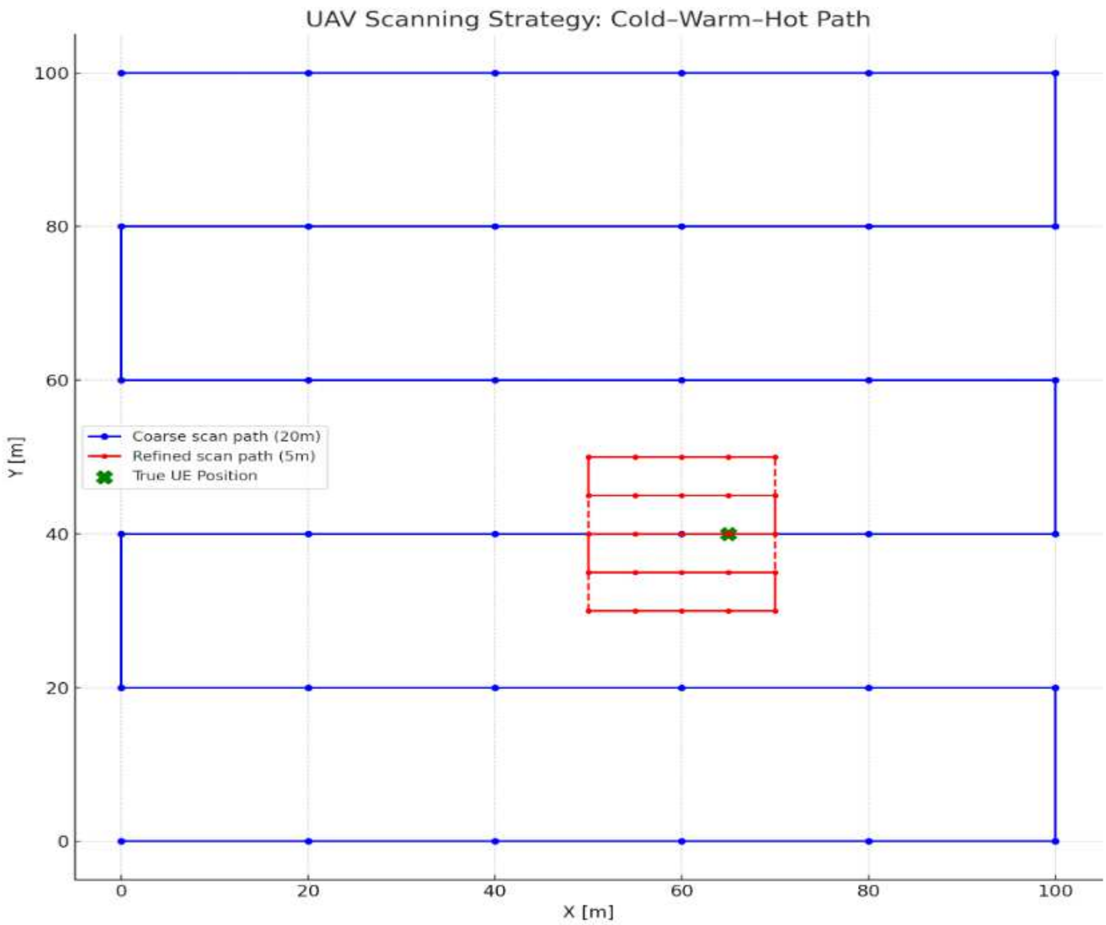

Figure 3.4: UAV scanning path using Cold–Warm–Hot strategy.

the 5 m refinement grid).

2. Refined RSS heatmap after adaptive scanning: it contains more densely sampled measurements in the warm cells of interest, providing high spatial resolution and clear identification of the UE location (see Figure 3.6).

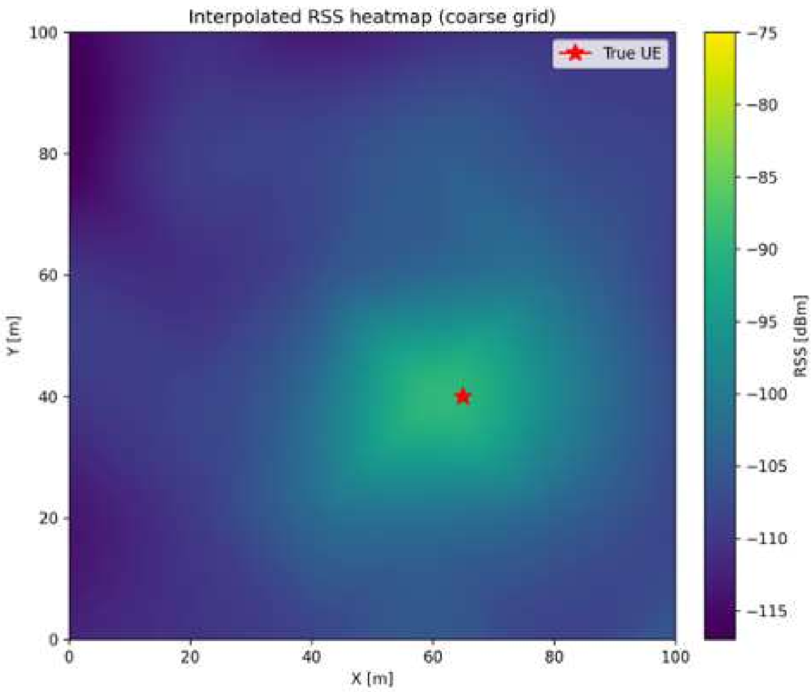

Figure 3.5: RSS heatmap (20 m step).

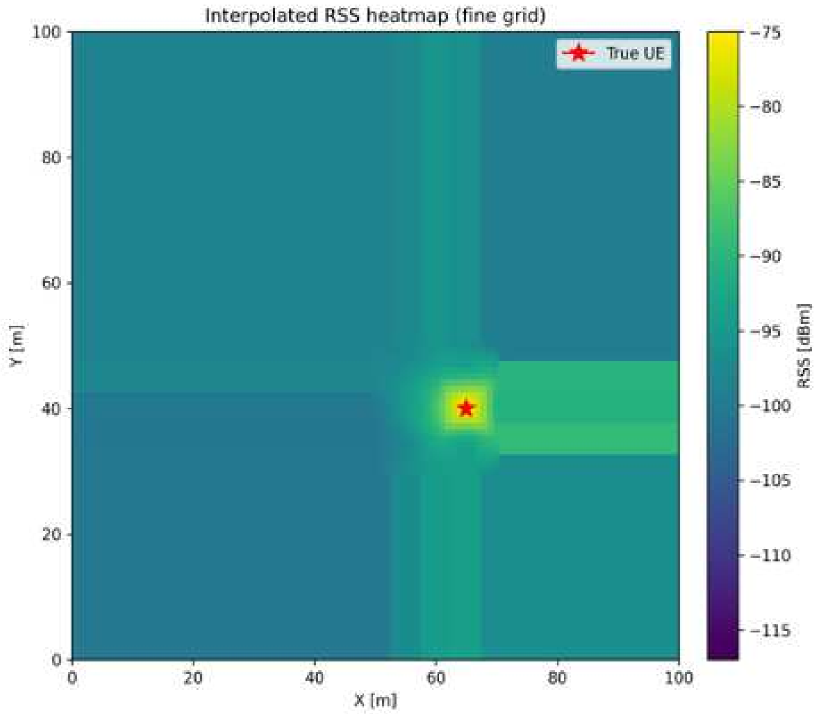

Figure 3.6: Refined RSS heatmap.

These visualizations confirm that the cold–warm–hot strategy results in improved localization accuracy and optimal measurement density. The proposed overflight algorithm forms the basis for the subsequent stages in NLoS conditions.

3.4 NLoS-aware extension

Effect of NLoS on RSS and measurement accuracy. NLoS propagation reduces the mean received power and increases its variability. Relative to the LoS model in (3.5), each traversed obstacle adds a material-dependent penetration loss, shifting the average RSS by $-\sum L_m$. In addition to this deterministic attenuation, multipath and shadowing are stronger in NLoS: the shadowing variance is typically higher than in LoS, and temporal fluctuations become more pronounced as the UAV moves [8, 30]. Averaging multiple snapshots mitigates small-scale fading, but the NLoS bias persists unless compensated; this motivates the material-aware correction in (3.6) and Table 3.1.

To emulate realistic propagation, we extend the basic Line-of-sight propagation (LoS) log-distance model by introducing obstacles with material-dependent penetration losses. The 2D 100 x 100 m search area contains a set of axis-aligned rectangular blocks, representing buildings, obstructions, rubbles, etc., each labeled by material $m \in \{\text{glass}, \text{ IRR glass}, \text{ concrete}, \text{ wood}\}$. A drone measurement at position $\mathbf{p}$ is flagged as LoS if the segment between $\mathbf{p}$ and the UE does not intersect any

rectangle; otherwise it is NLoS.
As mentioned earlier, the LoS RSS model is

$$\mathrm{RSS}_{\mathrm{LoS}}(\mathbf{p}) \;=\; \mathrm{RSS}_0 \;-\; 10\,n\,\log_{10}\!\left(\frac{d(\mathbf{p})}{d_0}\right) \;+\; X_\sigma, \tag{3.5}$$

where $d(\mathbf{p})$ is the distance to the UE, n is the path-loss exponent, and $X_\sigma \sim \mathcal{N}(0, \sigma^2)$ models log-normal shadowing (in dB).
For NLoS we subtract the cumulative penetration loss of the intersected materials:

$$\mathrm{RSS}_{\mathrm{NLoS}}(\mathbf{p}) \;=\; \mathrm{RSS}_{\mathrm{LoS}}(\mathbf{p}) \;-\; \sum_{m \in \mathcal{M}(\mathbf{p})} L_m(f), \tag{3.6}$$

where $\mathcal{M}(\mathbf{p})$ is the set of materials crossed by the line segment (drone $\to$ UE), and $L_m(f)$ is the penetration loss (in dB) at frequency f (GHz), as reported in Table 3.1. We adopt the standard piecewise-linear fits from [8]:

Table 3.1: Material penetration losses (3GPP TR 38.901) and values at f=3.5 GHz.

Material	$L_m(f)$ [dB]	At f=3.5 GHz
Standard multi-pane glass	$L_{\mathrm{glass}} = 2 + 0.2f$	2.7
IRR glass	$L_{\mathrm{IRR}} = 23 + 0.3f$	24.05
Concrete	$L_{\mathrm{conc}} = 5 + 4f$	19.0
Wood	$L_{\mathrm{wood}} = 4.85 + 0.12f$	5.27

Note: f in GHz.

We consider two scans: a coarse grid (20 m step) to detect the warm cell, then a refined grid (5 m step) around the warm center. For analysis we produce (i) a coarse RSS heatmap comparing LoS vs NLoS and (ii) a refined NLoS heatmap. We store per-point metadata and the total penetration loss $L_{\mathrm{pen}}(\mathbf{p}) = \sum_{m \in \mathcal{M}(\mathbf{p})} L_m(f)$ (Table 3.1). The ideally corrected RSS is $\mathrm{RSS}_{\mathrm{corr}} = \mathrm{RSS}_{\mathrm{raw}} + L_{\mathrm{pen}}$, an upper bound under perfect obstacle recognition (explained further in 4.6).

- Figure 3.7 — Coarse RSS heatmap (LoS vs NLoS): side-by-side maps; the NLoS panel overlays the obstacle rectangles.
- Figure 3.8 — Refined RSS heatmap with penetration losses: fine-grid heatmap around the warm center in the NLoS scenario (obstacles overlaid).

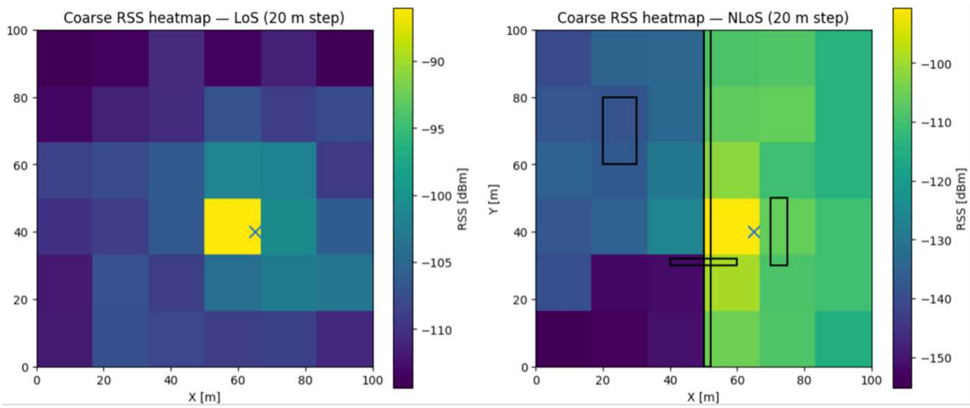

Figure 3.7: Coarse RSS heatmap (LoS vs NLoS).

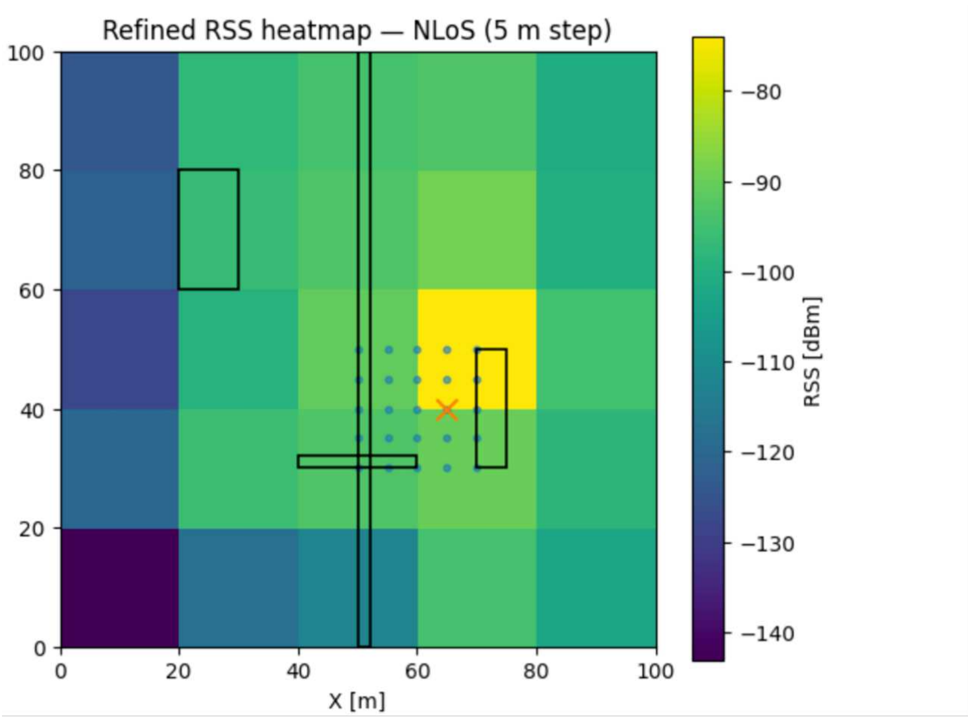

Figure 3.8: Refined RSS heatmap with penetration losses.

Why Computer Vision (CV)-based obstacle identification is needed. Maps generally provide footprints and materials for large buildings, but emergencies often introduce new, uncharted blockers (rubble piles, temporary structures, vehicles, partial collapses). Their positions and materials cannot be known a priori. On-board computer vision (e.g., semantic segmentation, object detection) is therefore required to identify blockers along the drone–UE path. The detected obstacles and their material classes feed the penetration-loss model (L_m) and enable obstacle-aware corrections such as RSS_{corr}, reducing NLoS-induced bias and improving localization accuracy.

The outputs of this section feeds the decision rule of Sec. 3.5.

3.5 Decision rule for refinement and positioning strategy

In this section, the "cold–warm–hot" flight logic is supplemented by a simple decision-making rule that selects a positioning strategy after a 20 m coarse scan. We deliberately do not tie this rule to a specific model: multilateration is only mentioned here as an optional fast refinement and is developed in detail in Chapter 4.

Note that the warm cell is still detected exclusively by the threshold rule in Eq. (3.3). The indicator introduced below does not redefine the warm cell; it only decides whether we can skip the refinement flyover and attempt a fast position estimate directly from the coarse map.

After the first exhaustive coarse scan phase, we decide whether to:

(a) immediately predict the UE location using multilateration based on the coarse scan results (we call it fast path (Sec. 3.5)), or

(b) perform a 5-meter refinement flyover (warm phase) and predict the UE location based on the refined heatmap peak.

After the warm cells have been identified, we compute indicators from the coarse map to select the branch:

Let $x_{\max}$ denote the coarse warm-center. We define the set of *anchor points* as a subset of coarse-grid measurement points around $x_{\max}$, used for subsequent estimation:

$$A \subset G, \qquad A = \{a_1, \ldots, a_M\},$$

where $M = |A|$ and each $a_i \in G$ is a coarse-grid waypoint with an averaged RSS.

Heat locality (H): We measure the spatial concentration of the warm region by inspecting the first neighborhood of the max-RSS cell on the 20 m grid. Specifically, we take a 30 m radius (i.e., the eight immediate neighbors on a 20 m grid) and compute the fraction of cells whose RSS exceeds $\overline{R}_{\text{global}} + \Delta$ (with $\overline{R}_{\text{global}}$ from Eq. (3.2)). We trigger fast path only if $H \geq 0.4$, i.e., at least 3–4 neighbors are warm.

Rationale for the H threshold. To avoid triggering multilateration on a spurious noisy spike, we require a minimum level of spatial consistency in the coarse RSS map. Specifically, we compute the heat locality H as the fraction of the eight immediate neighbors (30 m radius) around the max-RSS cell that are also classified as warm ($R(p_i) > \bar{R} + \Delta$). The fast path is enabled only if $H \geq 0.4$, i.e., at least 3 of the 8 neighbors confirm the peak.

This threshold is justified by a simple statistical argument. A cell is marked warm if its average RSS exceeds the global mean by $\Delta \approx 5\,\mathrm{dB}$. Given short-term fading $\sigma \approx 2\,\mathrm{dB}$ and averaging $K = 3$ RSS measurements per point, the chance that an individual cell is falsely declared warm is $p \approx 0.05$. If no true hotspot exists, the number of warm neighbors is $X \sim \mathrm{Binomial}(n{=}8, p)$. The false-alarm probability $\Pr\{X \geq 3\} = \sum_{k=3}^{8} \binom{8}{k} p^k (1-p)^{8-k}$ evaluates to ≈ 0.006 for $p = 0.05$, and remains below 4% even for pessimistic $p = 0.10$. Therefore, the rule $H \geq 0.4$ ensures that the fast path is triggered only when the maximum belongs to a spatially coherent warm region rather than to a random fading outlier. This lightweight criterion offers strong protection against false positives while keeping the decision rule simple and robust.

NLoS fraction (N): Using the obstacle map from the CV module (introduced in Sec. 3.4), and the anchor set $A = \{a_1, \ldots, a_M\}$ defined above, we trace the segment $a_i \to x_{\max}$ for each anchor a_i. If it crosses at least one marked polygon (glass/IRR/concrete/wood), we mark the ray as NLoS. Then

$$N = \frac{\left|\{\, a_i \in A \ :\ \text{segment } a_i \to x_{\max} \text{ intersects an obstacle} \,\}\right|}{M}, \tag{3.7}$$

where $M = |A|$ is the number of anchor points, a_i are their positions, and $x_{\max}$ is the coarse warm-center.

Choice of the N threshold. The fraction of obstructed anchor–UE rays (N) is a key indicator of whether RSS-to-range multilateration can be trusted. Each NLoS ray adds a material-dependent penetration loss $L_{\mathrm{pen}}(f)$ that, when mapped back to distance, makes the estimator interpret the same RSS as if the UE were κ times farther away, with $\kappa = 10^{L_{\mathrm{pen}}/(10n)}$. For example, at $f = 3.5\,\mathrm{GHz}$ with concrete ($L_{\mathrm{pen}} \approx 19\,\mathrm{dB}$) and $n = 2$, this yields $\kappa \approx 3.16$. When only a few rays are affected, the geometry remains approximately consistent; however, as N grows, the least-squares solution is pulled away from the scene and quickly diverges.

This behavior is confirmed by a Monte Carlo sweep with $M = 9$ nearest anchors and $\sigma = 2\,\mathrm{dB}$ shadowing. Figure 3.9 shows that for $N \leq 0.2$ the WLS error remains at the meter level, but at $N \approx 0.3$ a sharp regime change occurs: the RMSE escalates from $\sim$12 m at $N = 0.2$ to $\sim$26 m at $N = 0.3$, and exceeds tens of meters for $N \geq 0.4$. The knee of the curve is therefore around $N^\star \approx 0.3$.

An independent first-order analysis leads to the same boundary: the expected systematic bias scales with the obstructed-ray fraction as $N L_{\mathrm{pen}}$. For concrete ($L_{\mathrm{pen}} \approx 19\,\mathrm{dB}$) and $N = 0.3$, this amounts to $\approx 5.7\,\mathrm{dB}$, already exceeding the warm-cell threshold $\Delta \approx 5\,\mathrm{dB}$ used in Sec. 3.2. Beyond this regime, the structural bias dominates random shadowing and the WLS assumptions cease to hold.

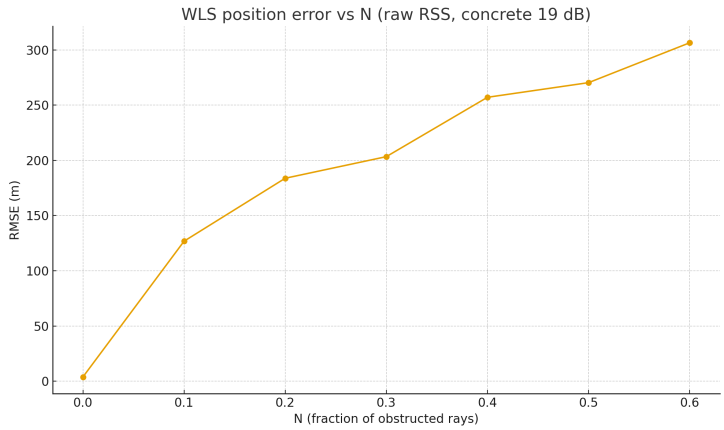

Figure 3.9: RMSE of WLS multilateration as a function of the obstructed-ray fraction N (Monte Carlo simulation, $M = 9$ anchors, $\sigma = 2$ dB, concrete wall with $L_{\text{pen}} \approx 19$ dB at $f = 3.5$ GHz). A clear knee appears at $N \approx 0.3$: for $N \leq 0.2$ the error remains at meter level, while for $N \geq 0.3$ the RMSE escalates rapidly to tens of meters. This empirical threshold confirms the decision rule of Sec. 3.5, where multilateration is avoided when $N \geq 0.3$ unless material-aware correction is available.

CV confidence notation. For each obstacle polygon intersected by a ray, the CV module (Sec. 3.4) outputs a material class and a confidence score $c_j \in [0, 1]$ (e.g., class-posterior). We call a label *confident* if $c_j \geq \gamma$; unless stated otherwise, we use $\gamma = 0.9$. Material-aware RSS correction along a ray is applied only if all intersected obstacles on that ray have confident labels.

Thus, the decision rule will be the following:

- **Fast path (coarse-grid multilateration).** Choose this path only if the coarse map is locally consistent and NLoS is limited: (a) $H \geq 0.4$ *and* $N < 0.3$; *or* (b) $H \geq 0.4$ and $N \geq 0.3$, but after applying obstacle-aware RSS correction on the intersected rays with confident CV material labels (see below), the corrected NLoS fraction drops below the threshold (i.e., $N_{\text{corr}} < 0.3$).
- **Robust path (default).** Otherwise, perform the 5 m refinement and use the refined heatmap peak as the estimate (room-level accuracy).

You can see the decision flow for fast and robust path based on heat locality (H) and NLoS fraction (N) on Fig. 3.9.

Multilateration is normally avoided when $N \geq 0.3$, since raw RSS distances are dominated by systematic NLoS bias. The heatmap, instead, relies on relative RSS in a local neighborhood: NLoS mainly adds a roughly constant L_{pen} dB offset behind a barrier, which depresses levels but preserves the local maximum near the UE (especially after the 5 m refinement). In contrast, multilateration converts that biased RSS into ranges; an NLoS loss scales distances by

$$\kappa = 10^{L_{\text{pen}}/(10\,n)}, \tag{3.8}$$

so when a sizable fraction of rays are biased (or one wall blocks most of them) the weighted LS solution is pulled far from the true position. However, if confident CV labels ($c_j \geq \gamma$) allow us to identify the obstacle material and apply penetration-loss correction (Sec. 3.4), the fast path (multilateration) can still be executed even when $N \geq 0.3$, as corrected ranges restore a consistent geometry.

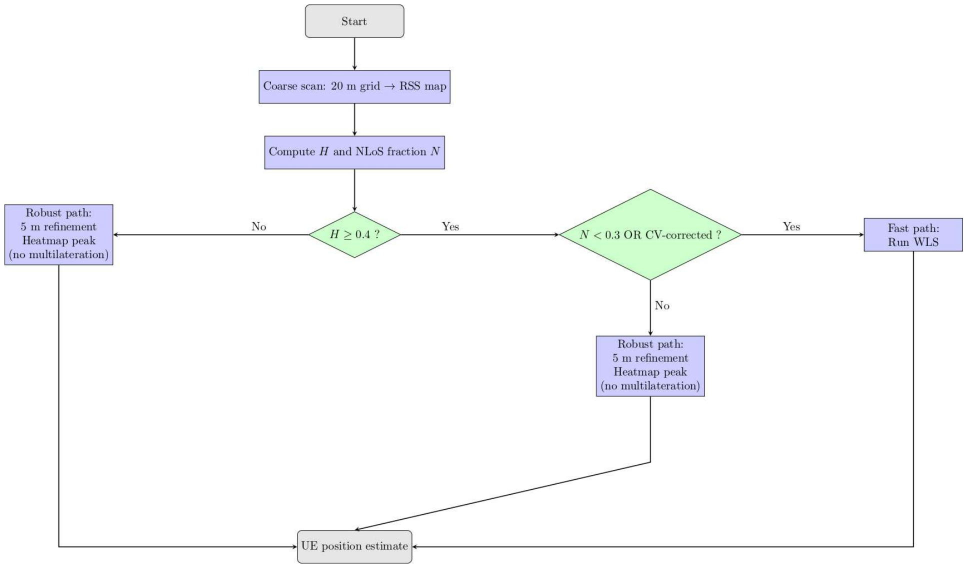

Figure 3.10: Decision flow for fast vs. robust path based on heat locality (H) and NLoS fraction (N).

4

Positioning Algorithm Based on RSS Data

This chapter formalizes RSS-based localization for our UAV testbed. Section 4.1 motivates RSS measurements (from PRACH) for infrastructure-light positioning. Section 4.2 outlines two complementary estimators used in our pipeline: a heatmap (local peak of relative RSS, robust path) and RSS-to-range multilateration (WLS, fast path). Section 4.3 details the practical WLS implementation. Section 4.4 defines accuracy metrics and discusses dominant error sources. Section 4.5 analyzes how NLoS bias breaks multilateration and motivates corrections. Sections 4.6–4.7 formalize material-aware RSS correction and the gating rule used in the decision logic. Section 4.8 summarizes limitations and practical considerations.

4.1 Introduction to RSS-Based Localization

Localization based on RSS is one of the most suitable approaches in wireless positioning systems. Main advantages of this method include its low computational complexity, possibility for integration in the existing wireless protocols, and no need for additional hardware [30].

Compared to the ToA and AoA based methods that require strict synchronization of the devices or specific antennas, the RSS approach uses only the signal power level which decays with increasing distance from the transmitter. That makes RSS very suitable for emergency scenarios when fast network deployment is needed using drones with a gNB installed on it.

In this project, RSS data are extracted from the PRACH channel which is used by UE for initiation of the network access procedure. As discussed in Chapter 2, PRACH plays a key role in the initialization of communication between the UE and the base station, especially in the uplink direction. Its ability to be transmitted without prior network connectivity [31] makes it particularly useful in emergency and unstructured scenarios. In this research, we use PRACH messages as a source of RSS measurements, which not only allows us to detect the presence of devices but also to estimate their relative position based on the received signal strength.

Therefore, the measured power of PRACH can be used for a UE distance estimation using path-loss models. These distance estimates are then fed to localization algorithms such as trilateration, which will be discussed in the following sections.

4.2 Overview of RSS-based localization approaches

We consider two complementary ways to turn UAV RSS measurements into a position estimate:

- heatmap-based localization, which relies on relative RSS patterns and selects the peak inside the refined scan; and
- RSS-to-range multilateration, which converts RSS to distances and solves a WLS system. In our pipeline (Section 3.5), multilateration is used only in the fast path of the decision rule, while the default (robust) path outputs the refined heatmap peak.

4.2.1 Heatmap-based localization (relative RSS)

At the first stage, the drone scans the area of interest on a grid with a step of 20 meters, recording RSS values obtained from the PRACH signal. After that, a detailed scan (5-meter step) is performed in the zones where increased signal strength was recorded ("warm zones"). The resulting measurements are interpolated or visualized as a spatial RSS map, where the color intensity reflects the signal strength *(see Chapter 3 for the flight logic and detection thresholds)*.

In this case the UE position is estimated as the point with the maximum RSS value. This method does not require knowledge of an accurate signal propagation model and is highly robust to interference; NLoS bias (a roughly constant dB offset) reduces all RSS levels by nearly the same amount but typically preserves the local maximum. It is particularly useful under conditions of limited information and lack of accurate synchronization. Even though it delivers room-level accuracy only (as shown in our experiments in Chapter 5), it is more than enough for our goals.

When materials are recognized, we apply an obstacle-aware correction (Sec. 3.4) prior to any range conversion: for a ray $a_i \rightarrow$ UE crossing labeled obstacles, add back the cumulative penetration loss $L_{\text{pen}}(f)$ to the measured RSS. This sets an upper bound on the achievable accuracy (Sec. 4.6), since real recognition is imperfect.

4.2.2 RSS-to-range multilateration (WLS)

When the fast branch of Section 3.5 is selected, we convert RSS to ranges and solve a WLS multilateration problem to obtain a coordinate-level estimate.

For each anchor $\mathbf{a}_i$ with RSS measurement r_i (in dBm) we use the log-distance model. If the ray $\mathbf{a}_i \rightarrow \text{UE}$ crosses labeled obstacles, we apply the correction (Section 4.6):

$$r_i^{\text{corr}} = r_i + L_{\text{pen}}(f), \tag{4.1}$$

where $L_{\text{pen}}(f) \equiv L_{\text{pen}}(a_i; f) = \sum_{m \in \mathcal{M}(a_i \to x_{\max})} L_m(f)$ (see Sec. 3.4 and Table 3.1). In Sec. 3.4 the corrected RSS was used for upper-bound analysis on heatmaps; here the same penetration-loss term is applied *per anchor* as an operational pre-correction before RSS-to-range conversion. In practice, we gate this correction by CV confidence (Sec. 3.5): it is applied only if all intersected obstacles have $c_j \geq \gamma$, otherwise $L_{\text{pen}}(a_i; f) = 0$. Optionally, after the first WLS solution $\hat{\mathbf{p}}$ we recompute L_{pen} along $a_i \to \hat{\mathbf{p}}$ and re-solve once (one-step refinement).

Otherwise $r_i^{\text{corr}} = r_i$. The range is then

$$d_i \;=\; d_0\, 10^{\frac{\text{RSS}_0 - r_i^{\text{corr}}}{10\,n}}, \tag{4.2}$$

where r_i is the measured RSS at anchor i, RSS_0 is the reference level at d_0 (we use $d_0 = 1\,\text{m}$), and n is the path-loss exponent.

WLS solver. With $M \geq 4$ non-collinear anchors we linearize by differencing to $\mathbf{a}_1$ and solve

$$2\,(\mathbf{a}_i - \mathbf{a}_1)^\top\, \hat{\mathbf{p}} \;=\; \left\|\mathbf{a}_i\right\|^2 - \left\|\mathbf{a}_1\right\|^2 \;+\; d_1^2 - d_i^2, \qquad i = 2, \ldots, M, \tag{4.3}$$

for the UE position $\hat{\mathbf{p}}$, by weighted least squares (details in Section 4.3) with

$$w_i \;=\; \frac{1}{d_i^2 + \varepsilon}, \tag{4.4}$$

where $\varepsilon > 0$ is a small regularization constant (in m^2) that prevents unbounded weights for very small d_i and improves numerical conditioning. In practice we use $\varepsilon = 1\ \text{m}^2$ (robust default) This emphasizes nearer anchors that carry higher SNR and smaller log-distance variance.

Linearization using anchor point differences (4.3) is a classic approach to multilateration: we subtract the range equation from the reference anchor point to obtain a linear system with an unknown position, and solve it using the WLS method [7].

Multilateration assumes a single source and unbiased ranges. Under heavy NLoS, raw RSS induces a systematic bias that stretches ranges and breaks the LS geometry (Section 4.5). In such cases our pipeline switches to the robust branch: 5 m refinement and the refined heatmap peak.

Heatmaps provide reliable localization that is ready for use in mixed-visibility conditions, while multilateration offers more accurate coordinates only if its assumptions are correct (LoS-like or corrected RSS).

4.3 Practical implementation of RSS-based multilateration

We use multilateration as an alternative to the warm zone reginement module in our strategy. It is executed only when the decision rule of Section 3.5 selects the fast path.

Weighted least-squares multilateration Let $\{\mathbf{a}_i \in \mathbb{R}^2\}_{i=1}^M$ be anchor positions and let r_i be the RSS (in dBm) measured at $\mathbf{a}_i$. If the ray $\mathbf{a}_i \to$ UE crosses labeled obstacles, we apply the material-aware (oracle) correction:

$$r_i^{\text{corr}} = \begin{cases} r_i + L_{\text{pen}}(f), & \text{if materials on the ray are known,} \\ r_i, & \text{otherwise.} \end{cases}$$

Ranges are then obtained from the log-distance model (4.2)

The unknown UE position $\hat{\mathbf{p}} \in \mathbb{R}^2$ is obtained by solving the linearized system (4.3) in the weighted least-squares sense. Define the per-equation residuals for $i = 2, \ldots, M$:

$$e_i(\mathbf{p}) \;=\; 2\,(\mathbf{a}_i - \mathbf{a}_1)^\top \mathbf{p} \;-\; \Big(\|\mathbf{a}_i\|^2 - \|\mathbf{a}_1\|^2 + d_1^2 - d_i^2 \Big).$$

We estimate $\hat{\mathbf{p}}$ by

$$\hat{\mathbf{p}} \;=\; \arg\min_{\mathbf{p}} \sum_{i=2}^{M} w_i\, e_i(\mathbf{p})^2,$$

with weights w_i from (4.4). This weighting emphasizes nearer anchors, which typically provide higher SNR and smaller log-distance variance.

Algorithm.

1. If the coarse locality is insufficient ($H < 0.4$), or if the NLoS fraction remains high ($N \geq 0.3$) after applying only confident CV-based corrections, abort multilateration and use the refined heatmap peak (Sec. 3.5).
2. (Optional) Correct RSS if materials are recognized: $r_i \leftarrow r_i + L_{\text{pen}}(f)$.
3. Convert to ranges via (4.2).
4. Assemble the equations (4.3) for $i = 2, \ldots, M$ (differencing to anchor 1); compute the weights w_i via (4.4).
5. Solve the weighted least-squares problem $\min_{\mathbf{p}} \sum_{i=2}^{M} w_i\, e_i(\mathbf{p})^2$ and report $\hat{\mathbf{p}}$.

The full implementation of the algorithm is available at the project repository *.

*`https://github.com/amalikov2000/Design-and-Implementation-of-UE-Detection`

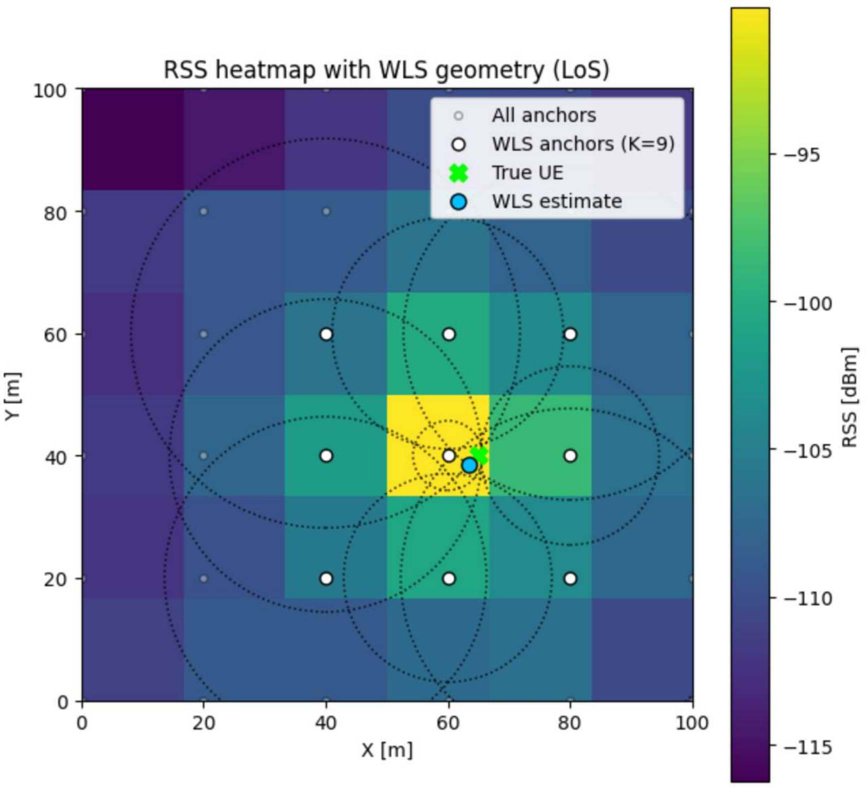

Figure 4.1: RSS heatmap with WLS geometry (LoS). Dotted circles show ranges d_i derived from RSS; grey dots are all coarse-grid anchors; white markers denote the M=9 anchors used by the WLS solver; the green cross marks the true UE; the blue dot is the WLS estimate.

On the coarse grid (20 m) we pick the M nearest anchors to the warm center and convert their RSS to ranges d_i. The position of the UE is estimated by numerically solving the multilateration problem. The localization error can be estimated as the RMSE between the true and estimated position.

4.4 Accuracy and practical aspects

We quantify how accurate the proposed pipeline is and what drives the error in practice. The system outputs either a refined heatmap peak (robust path) or a WLS multilateration estimate (fast path).

4.4.1 Metrics

Let $\mathbf{p}^\star$ be the true UE position and $\hat{\mathbf{p}}_k$ the estimate in the k-th Monte-Carlo run, with R the total number of runs. We report the mean-squared error (MSE), the root-MSE (RMSE), and—when needed—the mean absolute error (MAE):

$$\text{MSE} \;=\; \frac{1}{R}\sum_{k=1}^{R}\big\|\hat{\mathbf{p}}_k-\mathbf{p}^\star\big\|^2, \qquad \text{RMSE} \;=\; \sqrt{\text{MSE}}, \tag{4.5}$$

$$\text{MAE} \;=\; \frac{1}{R}\sum_{k=1}^{R}\big\|\hat{\mathbf{p}}_k-\mathbf{p}^\star\big\|. \tag{4.6}$$

These metrics are used consistently in both LoS and NLoS scenarios in this chapter.

4.4.2 What limits accuracy

- **Grid resolution (robust path).** With a 5 m refined grid, spatial quantization is on the order of 1–2 m; interpolation around the peak typically reduces it further when the warm region is compact (high H). Note: this term applies only when the robust path is selected (cf. Sec. 3.5); if $H \geq 0.4$ and the fast path is taken, refinement is skipped.

- **Shadowing/noise.** Random RSS fluctuations broaden the heatmap peak and add variance to ranges; averaging multiple snapshots per point is beneficial.

- **Calibration.** Errors in RSS_0, d_0 or n shift the distance scale; on-site calibration is recommended for the fast path.

- **NLoS bias (systematic).** Obstacles, blockages, or other possible obstructions introduce a positive range bias. To first order, when one inverts the LoS path-loss model, an extra loss L_{pen} dB leads the estimator to interpret the same RSS as if the UE were κ *times farther*:

  $$d_{\text{raw}} \;\approx\; \kappa\, d_{\text{true}}, \qquad \kappa \;=\; 10^{\,L_{\text{pen}}/(10\,n)}, \tag{4.7}$$

  where $L_{\text{pen}}(f)$ is the cumulative penetration loss along the ray. When a sizable fraction of rays is biased (high N), raw multilateration becomes unreliable due to this multiplicative range stretching. In such cases, the heatmap is generally more tolerant because a near-constant dB offset reduces all RSS levels but usually preserves the local maximum. However, if confident CV labels ($c_j \;\geq\; \gamma$) are available and penetration-loss correction is applied, the fast path (multilateration) can remain valid even for high N.

- **Altitude handling (in-model, no post-hoc correction).** All localization errors are reported in the 2D ground plane. We model path loss with horizontal distance d while absorbing the fixed UAV altitude h into the Close-In (CI) intercept: we choose the 3D reference distance $r_0 = \sqrt{d_{\text{ref}}^2 + h^2}$ at the actual UAV altitude so that altitude is captured by the intercept, while the slope remains a function of the ground-plane distance d. No post-processing subtraction of a 2D–3D offset is applied to the metrics.

4.5 NLoS influence on localization accuracy

In LoS, the logarithmic distance model with shadowing provides acceptable accuracy. However, in real-world conditions, propagation often becomes NLoS: the wave passes through obstacles (concrete, glass, IRR glass, wood), resulting in penetration losses unrelated to distance. This creates a systematic bias in RSS and leads to overestimation of range and position offset when using RSS-to-range multilateration.

According to 3GPP TR 38.901, typical penetration losses at $f \approx 3.5$ GHz are on the order of several to tens of dB (e.g., concrete $\approx$ 19 dB; IRR glass $\approx$ 23–25 dB; standard glass $\approx$ 2.7–5 dB; wood $\approx$ 4–6 dB). These values are far larger than random shadowing ($\sigma \approx 2$ dB), hence they dominate the error (Sec. 3.4).

A single dominant barrier that blocks most anchor–UE rays causes a nearly uniform multiplicative stretch (Fig. 4.2.) of the estimated ranges (4.7). In the linearized multilateration equations the right-hand side then scales roughly as κ^2, pulling the least-squares solution far from the scene (catastrophic RMSE for high-loss materials such as IRR glass and concrete). Therefore, in our pipeline we avoid multilateration on raw RSS when the NLoS fraction is high. We either (i) apply material-aware correction to RSS prior to range conversion (upper-bound case; Section 4.6), or (ii) fall back to the refined heatmap peak (robust path).

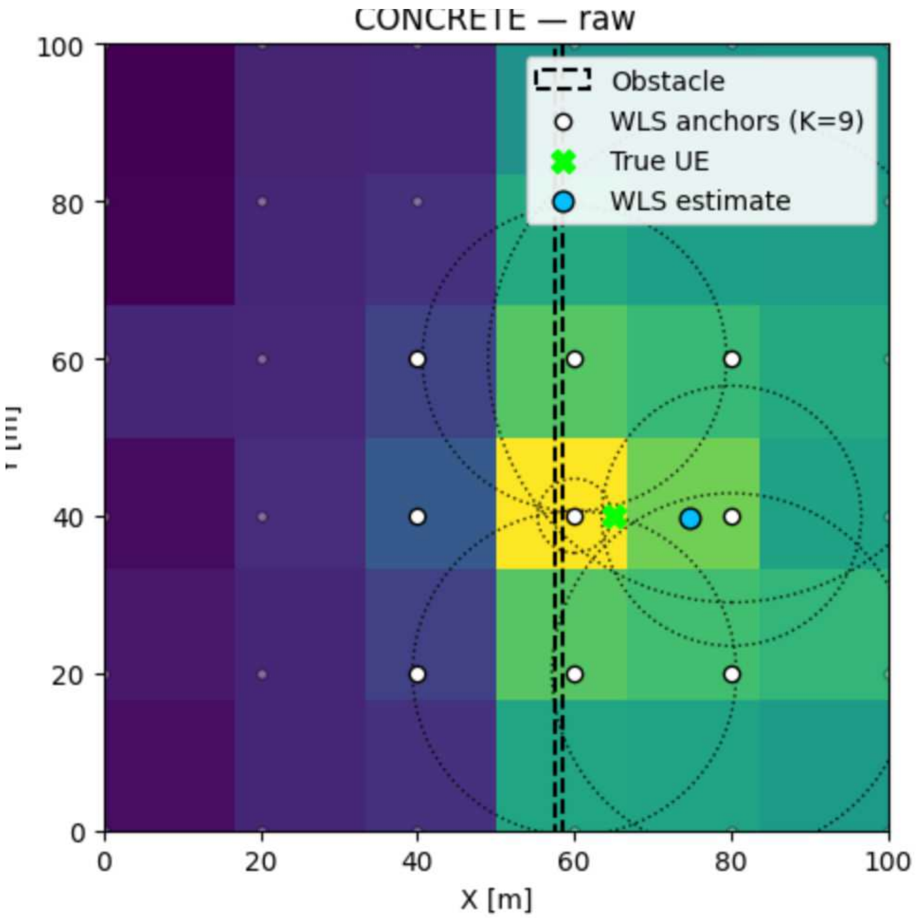

Figure 4.2: NLoS (raw): a vertical obstacle induces penetration loss along many anchor–UE rays, stretching RSS-derived ranges and breaking the WLS geometry; the estimate drifts away from the true UE.

4.6 Material-aware correction (formulation) and illustrative example

We quantify how penetration loss biases RSS-based localization and formalize a material-aware correction that uses obstacle labels (Sec. 3.4) before converting RSS to range. Quantitative evaluation (RMSE/STD across materials and altitude-offset metrics) is deferred to Chapter 5, Sec. 5.1.

4.6.1 Upper-bound (oracle) RSS correction

For an anchor $\mathbf{a}_i$ and a provisional target (UE), the measured RSS (in dB) is

$$r_i \;=\; \mathrm{RSS}_0 \;-\; 10\,n\log_{10}\!\left(\frac{d_i}{d_0}\right) \;-\; L_{\mathrm{pen},i}(f) \;+\; X, \qquad X \sim \mathcal{N}(0,\sigma^2), \tag{4.8}$$

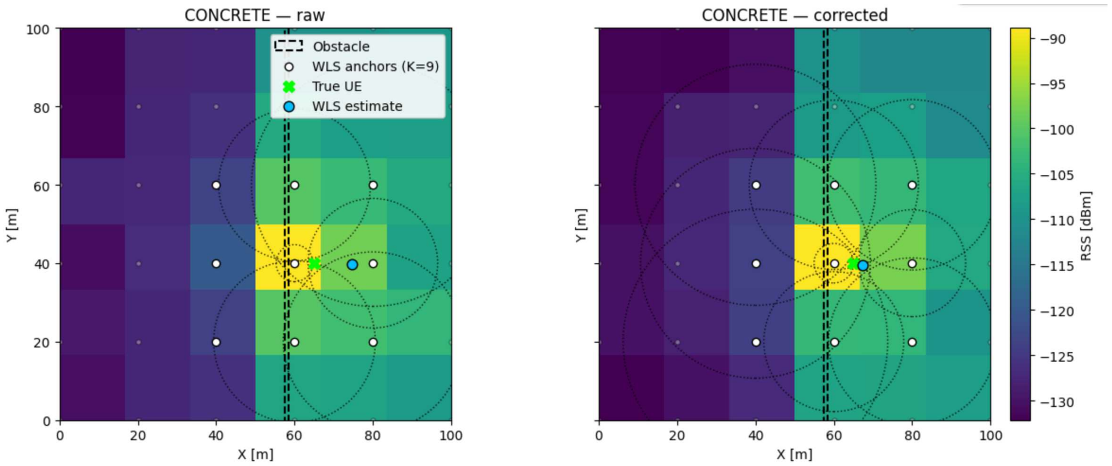

Figure 4.3: NLoS illustration (`concrete`): left—raw RSS causes biased ranges and WLS drift; right—oracle correction adds back $L_{\text{pen}}(f)$ on obstructed rays and restores LoS-like geometry.

where $L_{\text{pen},i}(f)$ is the cumulative penetration loss along the ray $\mathbf{a}_i \to$UE (zero in LoS). If crossed materials are known, we apply the oracle correction and only then convert RSS to range:

$$r_i^{\text{corr}} = r_i + L_{\text{pen},i}(f), \qquad d_i = d_0\, 10^{\frac{\text{RSS}_0 - r_i^{\text{corr}}}{10\,n}}. \tag{4.9}$$

This is an *upper bound* that assumes perfect recognition; otherwise we keep $r_i^{\text{corr}} = r_i$.

4.6.2 Illustrative geometry

Figure 4.3 shows a single-wall NLoS case (`concrete`): raw RSS induces a nearly uniform multiplicative stretch of ranges, which breaks the least-squares geometry; adding back $L_{\text{pen}}(f)$ per obstructed ray restores a LoS-like geometry. Comprehensive quantitative results are presented in Chapter 5 (Sec. 5.1).

4.7 RSS correction based on visual obstacle recognition

This work adopts an RSS correction mechanism based on recognizing the type of obstacle with an onboard computer-vision (CV) module. The CV system itself is not developed here; we assume a monocular camera and a standard semantic/instance segmentation network trained on urban scenes (e.g., CNN-based approaches as in [32], [33]). The camera image is geo-referenced to the ground plane using camera–IMU extrinsics to project detected polygons into the map frame.

Procedure (one pass). For each anchor a_i and a candidate UE position $\mathbf{p}^{(\text{cand})}$ (by default, the coarse/refined heatmap peak), we:

1. Cast the ground-plane ray $a_i \to \mathbf{p}^{(\text{cand})}$ and intersect it with CV polygons.

2. Keep only labels with confidence $\geq \gamma$ (we use $\gamma = 0.9$). Here $c_j \in [0, 1]$ is the per-polygon material confidence reported by the CV model (e.g., the posterior / softmax score for the predicted material class of polygon j); we accept a label if $c_j \geq \gamma$, with a conservative threshold $\gamma = 0.9$.

3. For every retained polygon, look up the penetration loss $L_m(f)$ from 3GPP TR 38.901 and sum along the ray to obtain the cumulative loss.

4. Correct the measurement by adding this cumulative loss in dB (cap at a plausible maximum, e.g., 30 dB to guard against projection errors).

5. Convert the corrected RSS to range using Eq. (4.2).

When we trust CV and take the fast branch. We estimate the NLoS fraction from confident labels and apply the decision rule

$$\textit{fast path (WLS)} \iff H \geq 0.4 \;\wedge\; \big(N < 0.3 \;\vee\; \text{CV-corrected}\big)$$

Here CV-corrected means that confident obstacle labels ($c_j \geq \gamma$, with $\gamma = 0.9$) are available, allowing us to apply material-aware RSS correction. Otherwise we abstain from multilateration and use the refined heatmap peak.

This CV-assisted correction is a semantic prior that "returns" obstacle-induced dB loss into the RSS reading. In this thesis we do not design or train the CV module; we merely define how its outputs (labels and confidences) are consumed by the localization pipeline. The oracle results of Section 4.6 provide an upper bound; with real recognition we expect performance in between raw and oracle curves, depending on γ and geo-referencing accuracy.

4.8 Discussion and limitations

Although the proposed obstacle-aware RSS correction improves positioning in NLoS, several practical limitations must be considered.

- Computer-vision reliability: The net performance hinges on correct material classification. Mislabels (e.g., glass $\rightarrow$ concrete) cause over / under-correction and can worsen accuracy. We therefore gate the fast branch by both the NLoS fraction and the availability of confident CV-based correction (Section 4.7): use WLS only if $H \geq 0.4$ and either $N < 0.3$ or CV correction is applied (with $c_j \geq \gamma = 0.9$ for contributing polygons). Otherwise fall back to the refined heatmap peak (Section 3.5).

- Spatio–temporal alignment: RSS samples and visual detections must be co-registered in space and time (camera–IMU extrinsics, latency compensation). Small misalignments due to motion or processing delays can lead to wrong ray–polygon intersections and biased $\widehat{L}_{\text{pen}}$.

- Barrier complexity: Our correction sums per-material losses along a straight ray. Real paths may traverse multiple layers, oblique incidences and partial occlusions; true loss depends on thickness and angle. Extending to multi-layer, angle-dependent losses is future work.
- Radio calibration: Errors in RSS_0, d_0, or n shift the distance scale and leak into WLS even in LoS. On-site calibration (or joint estimation of n) reduces bias in the fast branch.
- Anchor geometry and edge effects: WLS is sensitive to poor geometry (co-linear / weakly spread anchors) and border cases of the coarse grid; prefer central anchors or increase K when possible.

Despite these constraints, combining scene understanding with physical-layer models makes the pipeline more robust in mixed-visibility urban deployments. The oracle results in Section 4.6 set an upper bound; with real CV we expect performance between raw and oracle, governed by CV confidence, registration accuracy and the gating rule.

5 Simulation results

This chapter presents the results of the simulations that validate the proposed framework. We first establish a baseline at f=3.5 GHz comparing LoS with representative NLoS materials (E1), then study sensitivity to channel parameters n and σ (E2) and to calibration of RSS_0 (E3). Next, we quantify the geometry–cost trade-off by varying the number of coarse waypoints and the anchors used by WLS (E4), assess the benefit of temporal averaging per waypoint (E5), and examine frequency dependence across 2.6/3.5/4.9 GHz (E6).

5.1 Baseline evaluation (E1): LoS vs. NLoS materials

I begin by establishing a baseline for RSS→range WLS localization under LoS and representative NLoS materials. This evaluation also quantifies the benefit of applying a material-aware (oracle) correction (Sec. 4.6). Here is the experimental setup:

- area 100×100 m;
- coarse grid step 20 m;
- M=9 nearest anchors for WLS;
- f=3.5 GHz;
- log-distance path loss with lognormal shadowing σ=2 dB;
- UAV altitude h=100 m.

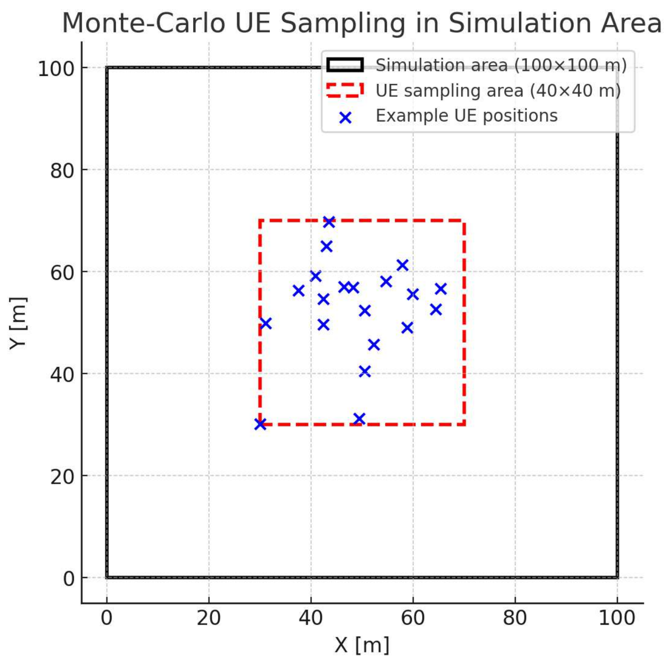

Figure 5.1: Monte-Carlo sampling of UE positions. The black square denotes the full 100×100 m simulation area, while the red dashed inner square ($[30, 70]^2$ m) indicates the region from which UE positions are drawn uniformly at random. Blue markers show example sampled positions.

Altitude-aware CI intercept (2D model). All geometry and metrics are computed in the 2D ground plane (horizontal distance d). To account for the fixed UAV altitude h in the path-loss model, we adopt the Close-In (CI) formulation with a 3D reference distance $r_0 = \sqrt{d_{\text{ref}}^2 + h^2}$ at the actual altitude. Thus, altitude is absorbed into the CI intercept, while the slope remains a function of the ground-plane distance d. This is consistent with the CI reference-distance formulation in 3GPP TR 38.901 and related literature [8, 34, 35]. No post-hoc 2D–3D offset subtraction is applied to the reported metrics.

We conduct R=100 Monte Carlo trials, where in each trial the position of the UE is selected randomly from the central region $[30, 70]^2$ m (see Fig. 5.1).

Restricting the sampling to this 40×40 m inner square prevents edge effects that could distort the geometry of the WLS solver. Materials are modeled according to the frequency-dependent penetration-loss fits in 3GPP TR 38.901, with IRR glass and concrete representing the strongest attenuation cases. For each scenario we report position RMSE/STD for both raw WLS and oracle-corrected WLS.

With a coarse grid step of 20 m (36 anchor points) and hovering time of 3–5 seconds per point, the coarse scan lasts about 6.3 minutes ($\approx$ 2.4 min hovering + $\approx$ 3.9 min transit) with a drone speed of 3 m/s.

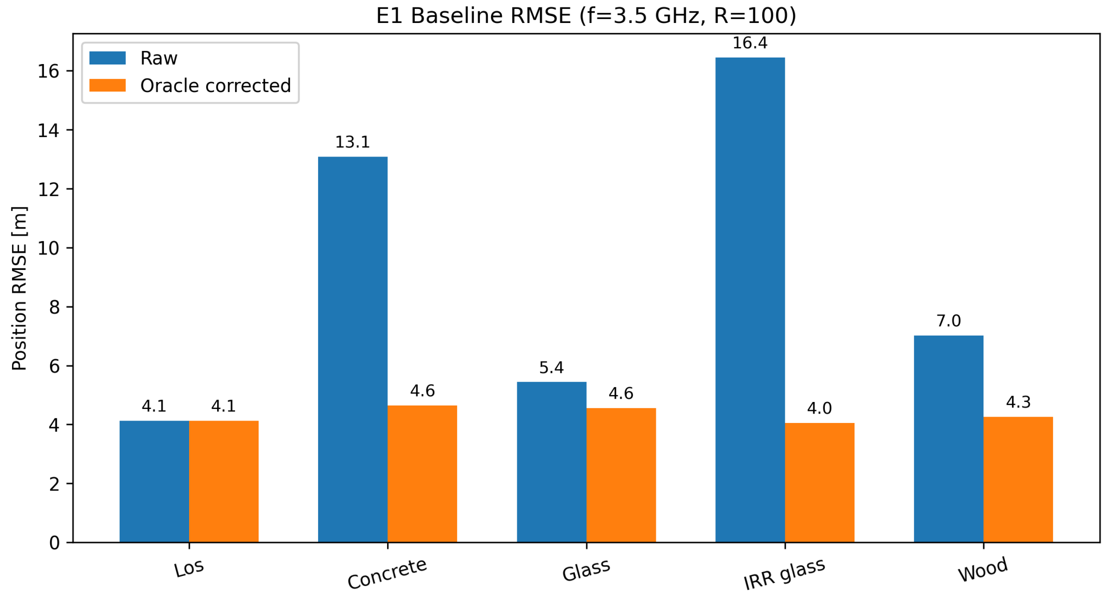

Figure 5.2: E1: Position RMSE (f=3.5 GHz, R=100). Oracle correction removes the NLoS bias across materials.

Table 5.1: E1: RMSE, STD and 95% CI at f=3.5 GHz (R=100, M=9).

Scenario	$\mathrm{RMSE}_{\mathrm{raw}}$ [m]	$\mathrm{STD}_{\mathrm{raw}}$ [m]	$\mathrm{CI}_{95,\mathrm{raw}}$ [m]	$\mathrm{RMSE}_{\mathrm{oracle}}$ [m]	$\mathrm{STD}_{\mathrm{oracle}}$ [m]	$\mathrm{CI}_{95,\mathrm{oracle}}$ [m]
LoS	4.1	1.5	0.3	4.1	1.5	0.3
Concrete	13.1	4.5	0.9	4.6	1.8	0.4
Glass	5.4	2.3	0.5	4.6	2.0	0.4
IRR glass	16.4	8.2	1.6	4.0	1.6	0.3
Wood	7.0	2.5	0.5	4.3	1.7	0.3

LoS vs NLoS. Under LoS the error is modest (RMSE $\approx$ 4.1 m). In NLoS, raw WLS degrades depending on material—concrete $\approx$ 13.1 m, glass $\approx$ 5.4 m, IRR glass $\approx$ 16.4 m, wood $\approx$ 7.0 m—because penetration loss biases RSS and stretches inferred ranges. Applying the oracle material-aware correction collapses all cases to $\approx$4.0–4.6 m (near-LoS), confirming that penetration loss is the dominant error source (Fig. 5.2, Table 5.1).

Summary. (i) LoS delivers the lowest error; (ii) raw WLS under NLoS suffers material-dependent bias; (iii) oracle correction brings performance back to $\sim$4–5 m across materials.

While oracle correction assumes perfect obstacle labels and exact penetration values, real-world performance will depend on the accuracy of the vision-based pipeline.

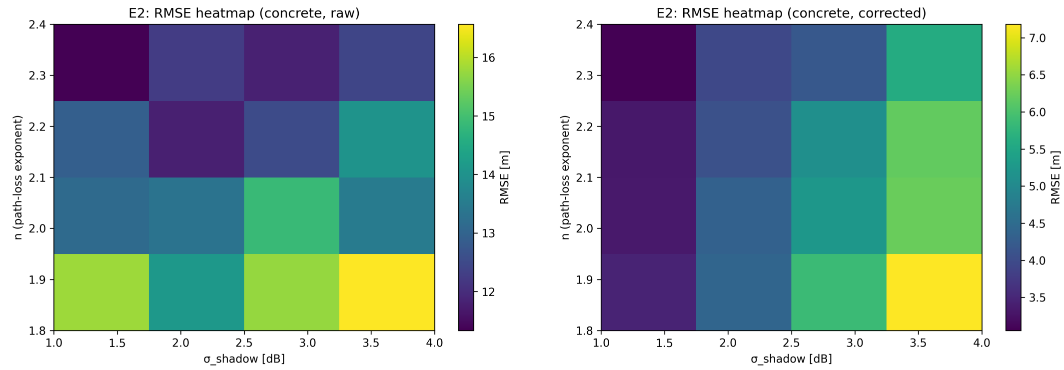

Figure 5.3: Channel sensitivity E2: heatmaps of RMSE as a function of path-loss exponent n (vertical axis) and shadowing σ (horizontal axis). Left: raw RSS without correction; Right: oracle correction with L_{pen} compensation.

5.2 Channel sensitivity (E2): effect of n and σ

In this experiment we observe how localization accuracy depends on two channel parameters: the path-loss exponent n (which controls how much power attenuates with distance) and the shadowing standard deviation σ (which models random fluctuations of RSS). The setup is a one-wall NLoS scene; for each (n, σ) pair we run R=100 trials, use the M=9 nearest anchors, convert RSS to ranges, and solve WLS in two variants: raw and oracle. Other parameters follow the baseline configuration of Sec. 5.1.

Raw case. Figure 5.3 (left) shows that RMSE grows almost monotonically with increasing σ, since a noisier RSS directly reduces the stability of WLS. At the same time, smaller n values (flatter distance law) make the ranges less discriminative, which also reduces accuracy. The worst performance is observed for low n and high σ.

Oracle correction. After applying material-aware correction (Fig. 5.3, right), the surface flattens: the strong NLoS bias is removed, and the residual dependence on n becomes weak. The RMSE levels approach those of LoS (around 3 - 5 m), with the main residual effect coming from random shadowing. This confirms that penetration losses, not channel variability, are the dominant error source in NLoS.

Summary. Overall, raw RMSE is highly sensitive to both parameters, while oracle correction brings the error close to the LoS floor. For consistency in the rest of the chapter we fix n=2.0 and σ=2 dB as default values.

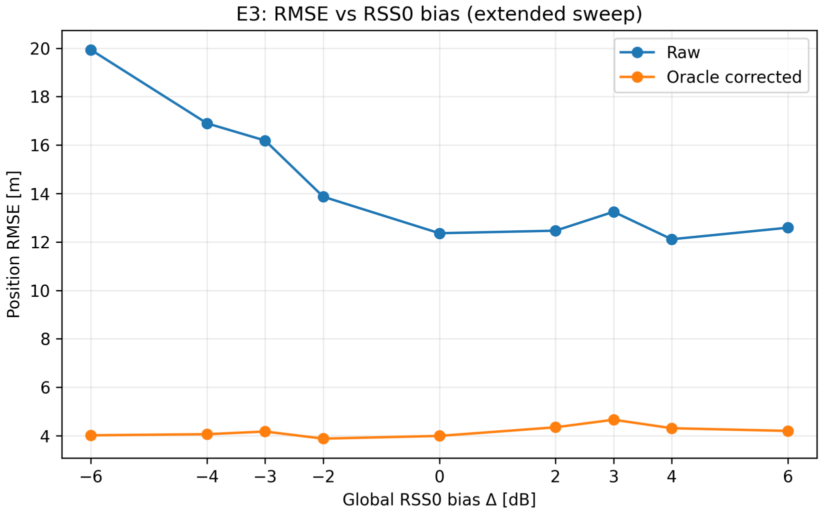

Figure 5.4: E3: RMSE versus global calibration bias ΔRSS_0 (concrete wall, f=3.5 GHz, R=100; extended sweep to $\pm$6 dB). Raw WLS is highly sensitive to Δ, while oracle-corrected results remain nearly flat at a few meters but still require decent calibration.

5.3 Calibration sensitivity (E3): global RSS_0 bias and per-anchor offsets

RSS_0 indicates the reference received signal strength at the reference distance $d_0 = 1$ m under LoS conditions. It serves as the anchor point of the log-distance path-loss model, and all range estimates are scaled relative to it. If RSS_0 is miscalibrated, every inferred distance is systematically shifted, leading to large localization errors. In this experiment I observe how calibration errors affect localization accuracy in a concrete-wall scenario. A global RSS_0 bias

$$\Delta \in \{-6, -4, -3, -2, 0, +2, +3, +4, +6\} \text{ dB}$$

is applied to all anchors, which rescales every inferred range by $10^{\Delta/(10n)}$. This operation expands or contracts all multilateration circles simultaneously.

Results. Figure 5.4 shows a clear and asymmetric sensitivity to the global offset. For the raw WLS, RMSE varies from about 20 m at $\Delta = -6$ dB down to $\approx$ 12–13 m for $\Delta \in [+3, +6]$ dB. This reduction for small positive Δ is specific to this geometry: a slight positive offset partly counteracts the NLoS–induced range stretch behind the concrete wall. However, the effect is accidental and not general, and the error remains one order of magnitude larger than in LoS-like conditions.

After oracle material correction, the curve becomes almost flat: RMSE stays within $\approx$ 4.0–4.8 m across the whole range ($\pm$6 dB), with a mild bump around $\Delta \approx +3$ dB and a return towards $\approx$ 4.2 m by $\Delta = +6$ dB. Thus, while penetration–loss compensation removes the dominant NLoS bias, large $|\Delta|$ still degrades accuracy slightly, confirming that a good RSS_0 calibration remains important even with correction.

Overall, these results highlight that material-aware correction can neutralize NLoS bias but cannot hide a global intercept error: keeping RSS_0 tightly calibrated is still necessary.

5.4 Geometry and flight budget (E4): grid density and number of anchors M

Scope. Unless otherwise stated, all results in this section refer to the coarse multilateration stage only (WLS on coarse-scan anchors), i.e., no warm-zone refinement. This isolates the impact of grid density and anchor count on the baseline geometry and cost.

In this experiment I study how the geometry of the coarse scan affects localization accuracy under concrete-wall conditions (f=3.5 GHz). I use the number of coarse waypoints $N_{\text{pts}} \in \{25, 36, 49, 121\}$, which directly reflects the operator cost and battery usage. In parallel, I vary the number of anchors used for WLS, $M \in \{6, 9, 12\}$. Increasing N_{pts} densifies the geometry and improves conditioning; increasing M adds equations and redundancy, but may inject low-SNR far anchors.

Effect of grid density (N_{pts}). Figure 5.5 shows monotonic gains as the coarse grid is densified. The largest drop occurs between N_{pts}=36 and 49 (former $s \approx 20$ m $\to$ latter $s \approx 15$ m on a 100×100 m area): raw RMSE improves substantially, while the corrected curves (dashed) move from $\sim$3–5 m down to $\sim$2.5–3.5 m depending on M. Further densification to N_{pts}=121 (former $s \approx 10$ m) continues to help but with diminishing returns.

Effect of M. For raw WLS, using too many anchors can hurt because far anchors are low-SNR and bias the fit (e.g., at dense grids, M=6 may slightly outperform M=9). After bias correction, however, M=9 consistently produces the lowest RMSE, while M=12 brings little benefit and sometimes degradation. This indicates that moderate redundancy ($M \approx 9$) is the best compromise between geometry and noise sensitivity.

Operational trade-off (time budget). To make costs explicit, I relate N_{pts} to coarse-scan time:

$$T = \frac{D(N_{\text{pts}})}{v} + N_{\text{pts}}\, t_h,$$

with serpentine coverage, horizontal speed v=3 m/s and per-point hover t_h=4 s (Sec. 5.1). Table 5.2 reports the resulting costs (CSV-backed), and Fig. 5.6 maps RMSE to flight time. Moving from N_{pts}=36 to 49 yields a clear accuracy gain at modest extra time; jumping to 121 nearly doubles T for smaller incremental gains. Note that all costs here refer to the *coarse scan*; any warm-zone refinement, when applied, adds a small, roughly constant overhead.

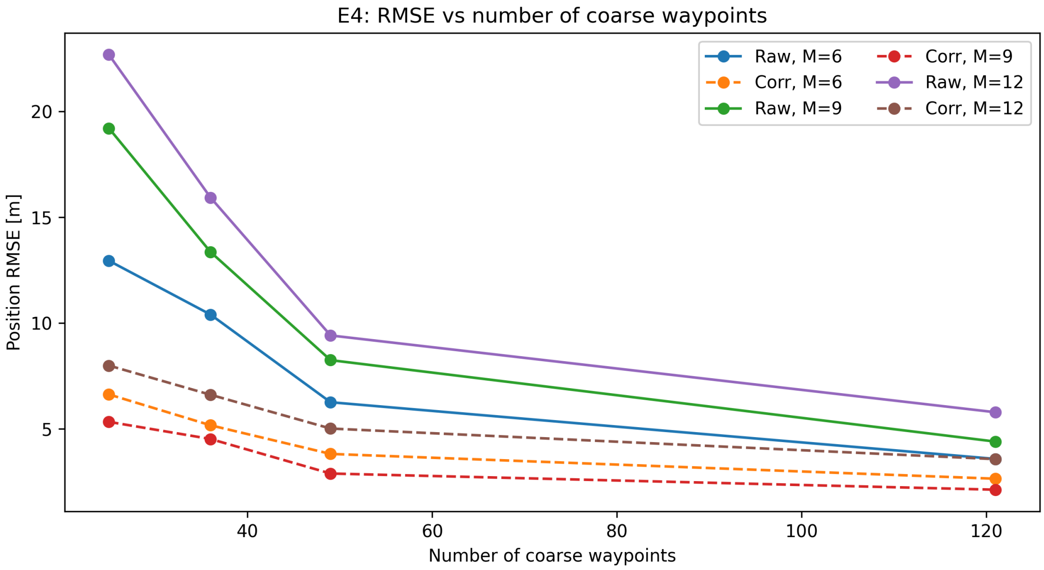

Figure 5.5: E4: Position RMSE vs number of coarse waypoints ($N_{\text{pts}} \in \{25, 36, 49, 121\}$), for $M \in \{6, 9, 12\}$. Dashed curves show oracle-corrected (bias-removed) RMSE; solid — raw WLS.

Table 5.2: Coarse-scan cost as a function of grid/waypoints (v=3.0 m/s, t_h=4.0 s/pt).

Step s [m]	Points N_{pts}	Path length D [m]	Flight time T [min]
25	25	600	5.0
20	36	700	6.3
15	49	720	7.3
10	121	1200	14.7

Design guidelines (multilateration only).

- **Grid density.** Target $N_{\text{pts}} \approx 49$ (former s≈15 m on 100×100 m). This delivers a strong accuracy gain over 36 points at a modest time increase, with clearly diminishing returns beyond.
- **Anchor count.** Use M≈9 anchors for WLS. Compared to M=6, it offers better corrected RMSE thanks to redundancy; M=12 is not recommended unless additional diversity is guaranteed (otherwise far low-SNR anchors can degrade raw WLS).
- **If battery- or time-limited.** N_{pts}=36 is an acceptable budget point (shorter T) at the cost of ∼20–40% higher raw RMSE vs. 49 points, depending on M.

Overall, for the coarse multilateration stage under concrete-wall conditions, a practical operating point is N_{pts}**≈49,** M≈9. This balances accuracy (∼3 m corrected, <10 m raw) and cost (T≈7–8 min at v=3 m/s, t_h=4 s/pt) while avoiding over-dense grids that double time for smaller gains.

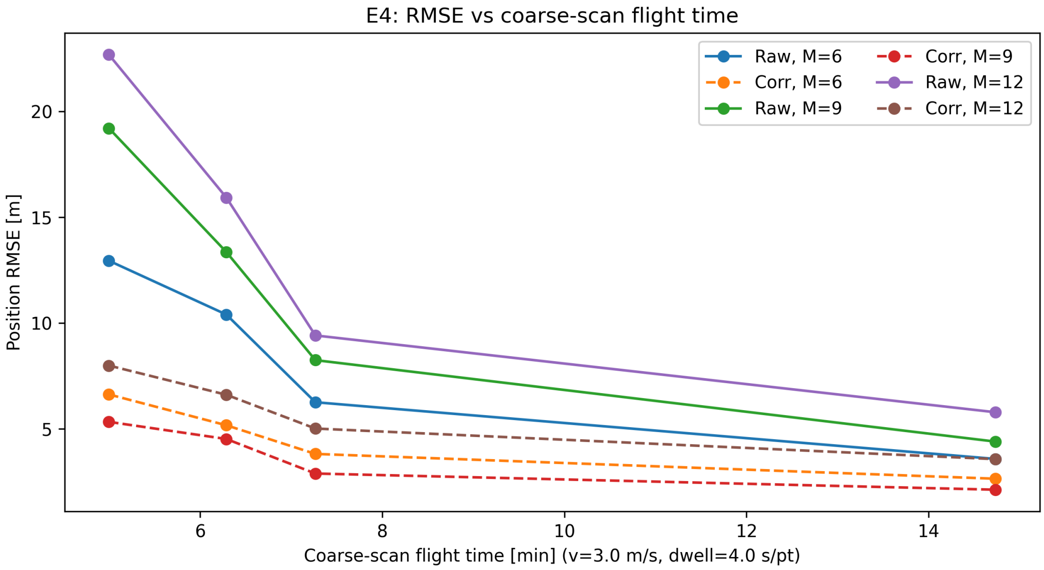

Figure 5.6: E4 (operational view): Position RMSE vs coarse-scan flight time (v=3.0 m/s, t_h=4.0 s/pt) for $M \in \{6, 9, 12\}$.

5.5 Temporal averaging (E5): K_{avg} samples per point

Scope. Results in this section refer to the *coarse multilateration stage only* (WLS on coarse-scan anchors), no warm-zone refinement. Concrete NLoS scene, sampling at 1 Hz.

In this experiment I evaluate the effect of temporal averaging of RSS samples. For each grid point, we collect $K_{\text{avg}} \in \{1, 3, 5, 7\}$ consecutive samples before converting RSS to ranges and applying WLS. Averaging suppresses random fluctuations, while systematic NLoS bias is unaffected.

Results. Figure 5.7 shows a clear reduction in RMSE when increasing K_{avg} from 1 to 3 and further to 5 (largest gain between 3 and 5). Beyond K_{avg}=5 the improvement saturates and at K_{avg}=7 RMSE slightly increases. This behaviour is consistent with

$$\text{RMSE}^2 = \text{bias}^2 + \text{var}, \qquad \text{var}(K_{\text{avg}}) \approx \frac{\sigma_{\text{eff}}^2}{K_{\text{eff}}},$$

where temporal correlation of RSS makes $K_{\text{eff}} < K_{\text{avg}}$; once the variance term is small, the NLoS bias dominates and additional averaging brings little benefit or can even hurt (drift/non-stationarity over a longer dwell).

Practical implication. Averaging increases hover time by $\Delta t = K_{\text{avg}}/1\,\text{Hz}$ per waypoint. The *elbow* is at $\underline{K_{\text{avg}}=5}$ (about 5 s dwell): it yields the lowest RMSE on our data with modest time cost. If battery/time is tight, $\underline{K_{\text{avg}}=3}$ is a good budget choice (most of the gain over K=1) without

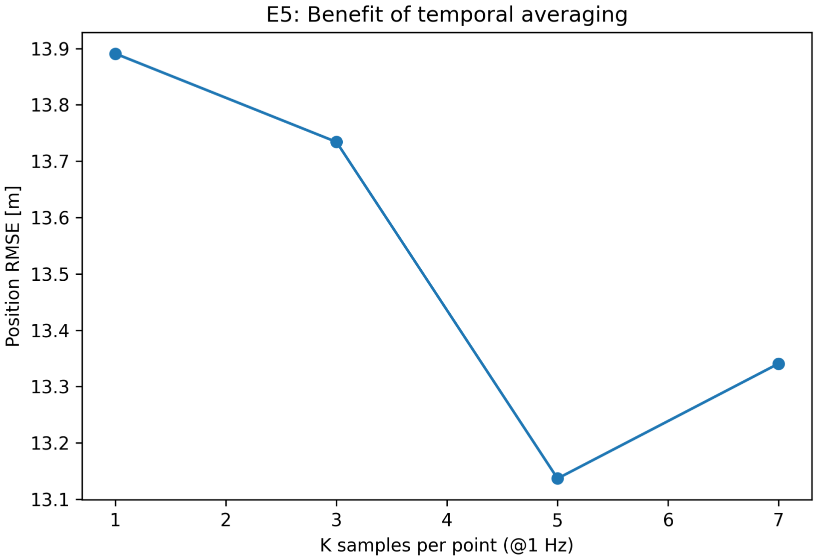

Figure 5.7: E5: RMSE versus the number of averaged samples K_{avg} at 1 Hz (multilateration only). RMSE drops notably from K_{avg}=1 to 3 and reaches its minimum at K_{avg}=5; at K_{avg}=7 a slight degradation appears.

risking non-stationarity.

5.6 Frequency dependence (E6): $f \in \{2.6,\ 3.5,\ 4.9\}$ GHz

We analyze how the carrier frequency affects NLoS penalties and localization accuracy across four materials (concrete, glass, IRR glass, wood) for $f \in \{2.6, 3.5, 4.9\}$ GHz. As f increases, penetration loss generally grows; however, the magnitude of raw errors depends on the material. In all cases, oracle correction collapses most of the error to a $\sim$4 m floor.

At 2.6 GHz (Fig. 5.8), penetration penalties are the lowest overall. Raw RMSE ranges from 4.9 m (glass) to 19.2 m (IRR glass), with concrete at 11.7 m and wood at 6.5 m. Oracle correction reduces all materials to $\approx$ 4.2–4.3 m.

At 3.5 GHz (Fig. 5.9), raw errors increase moderately relative to 2.6 GHz. IRR glass remains the harshest case (20.3 m), while glass and wood stay in the 5–7 m range; concrete rises to 12.9 m. Oracle correction again collapses the error to $\approx$ 4–4.4 m.

At 4.9 GHz (Fig. 5.10), concrete shows the largest increase (to 18.2 m, $\sim$ 36% higher than at 2.6 GHz), IRR glass stays near 20 m, while glass and wood grow only slightly (to 5.4 m and 7.0 m). Oracle correction remains effective with residuals around 4 m.

Summary and takeaways. (i) Material ranking is consistent: IRR glass and concrete are the worst cases; glass and wood are milder. (ii) Frequency effect is material-dependent: concrete raw RMSE increases notably with f (from 11.7 m at 2.6 GHz to 18.2 m at 4.9 GHz), while IRR glass remains $\sim$20 m across all bands; glass / wood vary within 5–7 m. (iii) Oracle correction consistently recovers most of the NLoS bias, yielding $\approx$ 4 m over all materials and bands.

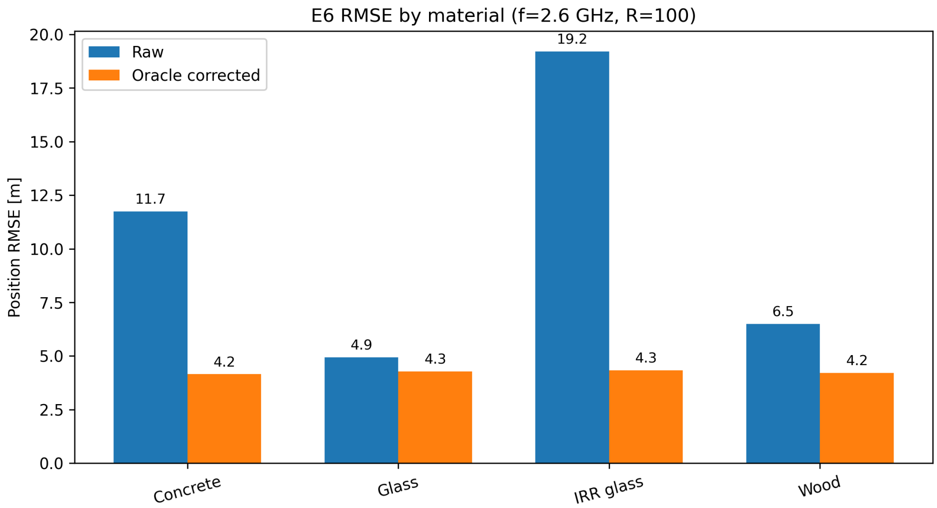

Figure 5.8: E6: RMSE by material at f=2.6 GHz (R=100). Raw: concrete 11.7 m, glass 4.9 m, IRR glass 19.2 m, wood 6.5 m. Oracle-corrected: $\approx$ 4.2–4.3 m.

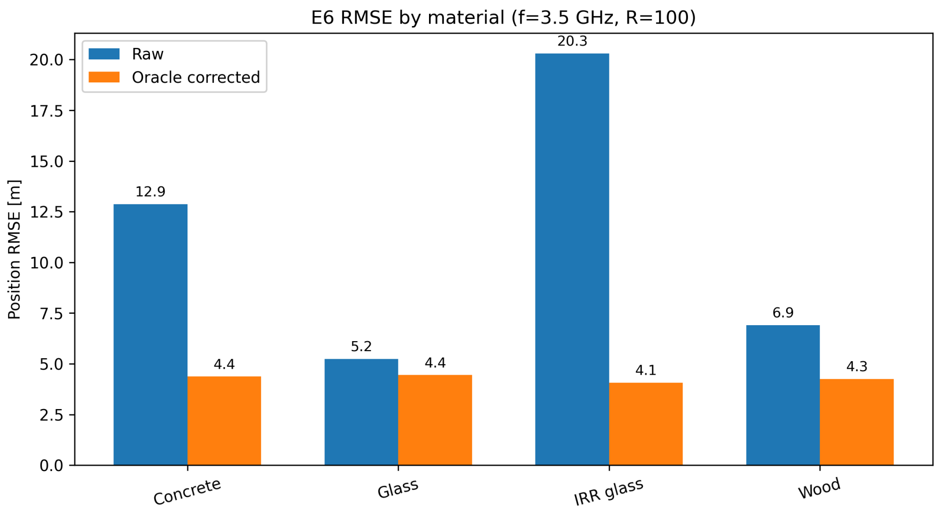

Figure 5.9: E6: RMSE by material at f=3.5 GHz (R=100). Raw: concrete 12.9 m, glass 5.2 m, IRR glass 20.3 m, wood 6.9 m. Oracle-corrected: $\approx$ 4.1–4.4 m.

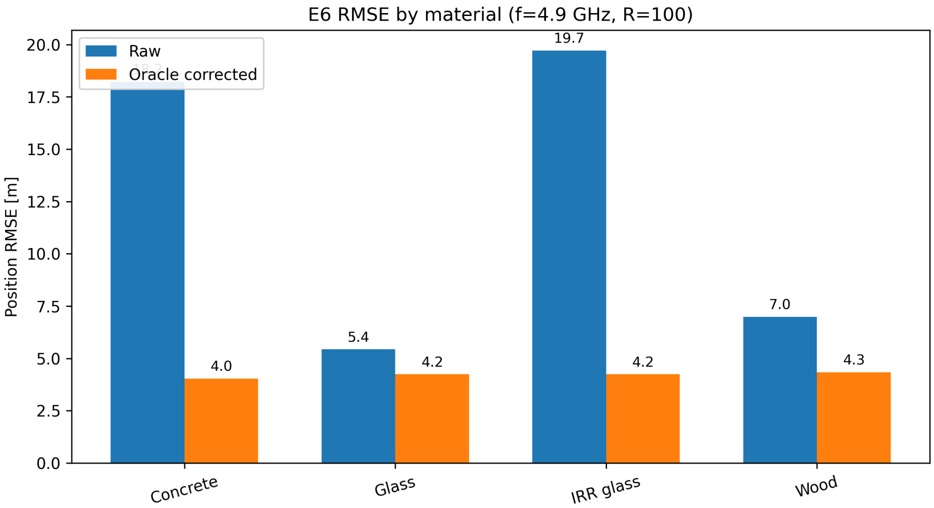

Figure 5.10: E6: RMSE by material at f=4.9 GHz (R=100). Raw: concrete 18.2 m, glass 5.4 m, IRR glass 19.7 m, wood 7.0 m. Oracle-corrected: $\approx$ 4.0–4.3 m.

5.7 Fast vs. robust at 15 m grid: head-to-head

Setup. Square area 100×100 m; carrier f=3.5 GHz; one concrete-like wall with penetration loss L_{pen}=9 dB for rays that cross it; log-distance path loss (n=2.0) with lognormal shadowing σ=2 dB. UAV altitude is handled via the CI intercept (2D ground-plane distances). The coarse scan uses a 15 m grid (N_{pts}=49). At each waypoint we average K_{avg}=5 temporal snapshots (1 Hz). The fast branch runs WLS over the M=9 closest anchors. The robust branch uses an RSS heatmap followed by 5 m refinement inside a 25×25 m warm zone. UAV speed v=3 m/s, hover t_h=4 s per point. Monte-Carlo: R=100 with UE uniformly sampled in $[30, 70]^2$ m.

We compare two anchor-selection policies for the fast branch: (A) **visibility-aware** (LoS anchors prioritized; CV-based per-ray correction enabled), and (B) **nearest-anchors** (geometrically closest anchors regardless of visibility; CV correction enabled). The CV correction is applied only to rays that cross the wall and pass a confidence gate.

Results (Table 5.3). Mode A (visibility-aware). Prioritizing LoS anchors yields M=9 LoS rays on average (blocked fraction 0.0), so CV correction is not needed (corrected fraction 0.0). In this regime, the fast branch attains RMSE $\approx$ 1.76 m, outperforming the robust branch ($\approx$ 2.06 m) with no warm-zone overhead.

Mode B (nearest-anchors). NLoS rays enter WLS (blocked fraction $\approx$ 0.10) and some get corrected by CV (corrected fraction $\approx$ 0.062), yet a residual bias remains. Fast degrades to RMSE $\approx$ 3.18 m, while robust remains stable at $\approx$ 2.06 m.

Why is FAST better than ROBUST in Mode A? In Mode A we prioritize LoS anchors, so WLS operates with M=9 unbiased LoS rays and temporal averaging (K_{avg}=5), which is the most favorable regime for multilateration. The robust branch, by design, optimizes raw RSS residuals on a discrete grid (heatmap and 5 m refinement) without CV pre-correction; hence, even in LoS-like scenes it retains a small quantization floor (≈1–2 m) and minor model mismatch, yielding ∼2.06 m rather than beating the ideal WLS. Robust is meant as a safety net for NLoS, not as a universal improvement over well-conditioned LoS multilateration.

Total time comparison. At the 15 m grid the coarse scan takes 10.10 min. FAST finishes here (total 10.10 min). ROBUST adds one warm-zone refinement (5 m over 25×25 m, ∼36 points), i.e., +3.93 min, for a total of ≈14.03 min. If multiple warm zones are refined, the ROBUST total scales linearly with their count.

Takeaways. When a sufficient number of LoS anchors is available, the fast WLS (15 m grid, M≈9, K_{avg}=3–5) achieves ∼1.7–2.0 m and should be preferred. If NLoS rays are unavoidable in WLS, the robust branch delivers ∼2.06 m consistently at the cost of ∼3.9 min per warm zone. A practical policy is to use FAST by default (15 m, M≈9, K_{avg}=3–5); switch to ROBUST when LoS coverage is insufficient or CV confidence is low. ROBUST offers accuracy that is stable to NLoS at the cost of ∼+3.9 min per warm zone, while FAST is superior in LoS-rich scenes.

Table 5.3: Fast vs. robust at 15 m (concrete-like NLoS, R=100). 'blocked" is the fraction of NLoS rays in WLS; corrected" is the fraction corrected by CV.

Mode	FAST RMSE [m]	ROBUST RMSE [m]	blocked frac.	corrected frac.	FAST total [min]	ROBUST total [min]
A: visibility-aware (CV on)	1.763	2.058	0.000	0.000	10.100	14.028
B: nearest-anchors (CV on)	3.182	2.061	0.099	0.062	10.100	14.028

5.8 Summary and discussion

Across all experiments, the main trend is clear: raw RSS→range WLS suffers from strong biases under NLoS conditions. When penetration losses are compensated by the material-aware oracle, errors come to a LoS levels (E1). Sensitivity to channel parameters also follows expectations: larger path-loss exponents n or higher shadowing variance σ both worsen accuracy(E2). Calibration is another critical factor: a misaligned global RSS_0 shifts all ranges coherently, highlighting the importance of proper calibration (E3). Geometry also matters: denser grids reduce RMSE, with M≈9 anchors giving the best balance between accuracy and stability (E4). Temporal averaging helps to suppress random noise, with $K_{\text{avg}} = 3$–5 samples giving stable estimates at a modest time cost (E5). Finally, frequency has a clear role: higher bands increase penetration losses and raw biases, while lower FR1 bands (e.g., 2.6 GHz) are more forgiving(E6).

Fast vs. robust (15 m grid). With visibility-aware anchor selection (prioritize LoS) and M=9, the fast branch attains ∼1.7–2.0 m without refinement; the robust branch is ∼2.06 m but adds ≈3.9 min per warm zone. If NLoS rays unavoidably enter WLS (nearest-anchor policy), fast degrades to ∼3.2 m while robust remains at ∼2.06 m. **Design rule:** use fast by default with 15 m grid, M≈9, and K_{avg}=3–5; fall back to robust when LoS coverage is insufficient or CV confidence is low.

Oracle vs. CV in practice. The "oracle" assumes perfect obstacle labels and exact L_{pen}; it is an upper bound. A CV pipeline provides probabilistic labels and approximate materials / thickness / angles. We apply per-ray correction only when confidence $c_j \geq \gamma$ and the predicted correction is within the model's validity; otherwise we keep the raw ray (possibly down-weighted) or switch to the robust path.

Outlook. Priorities are: (i) data-driven $L_{\text{pen}}(f, \text{material}, \theta)$, (ii) principled propagation of CV uncertainty to per-ray corrections and the confidence gate γ, (iii) a gating policy that defaults to fast and triggers robust on low-confidence or geometry-inconsistent corrections. With strong CV and calibrated L_{pen}, CV-driven correction can approach the oracle, but the oracle remains a theoretical ceiling.

6

Conclusion

Summary and contributions

This thesis designed and evaluated a two-branch UAV localization pipeline that couples a coarse RSS heatmap with a WLS multilateration and switches between them based on scene visibility. We ran a simulation campaign (E1–E6) to quantify accuracy, geometry, and budget trade-offs, and we reported operational metrics (flight time and number of waypoints). The main contributions are:

1. **Two-branch pipeline and switching.** A decision policy driven by the heatmap confidence H and the fraction of obstructed links N: when $H \geq 0.4$ and $N < 0.3$ WLS is preferred; otherwise a robust path is triggered. If per-ray visibility is available, material-aware correction enables WLS even at higher N.
2. **Geometry/budget study (E4).** For a $100 \times 100\,\mathrm{m}$ scene, densifying the coarse grid from $s{=}20$ to $15\,\mathrm{m}$ ($N_{\mathrm{pts}} : 36 \rightarrow 49$) substantially improves accuracy at modest extra time; adding more anchors beyond $M{\approx}9$ offers little benefit and may hurt due to far, low-SNR anchors.
3. **Channel sensitivities (E1–E3, E5–E6).** We quantified the impact of materials and penetration, path-loss/shadowing parameters, calibration biases, temporal averaging, and carrier frequency. Oracle material correction collapses most NLoS bias to a $\approx 4-5\,\mathrm{m}$ floor; nonetheless, large global RSS_0 biases remain harmful and motivate online calibration.
4. **Operationalization.** Accuracy is related to explicit costs: flight time and waypoint count. This yields simple recipes (grid/anchors/averaging) for planning missions under endurance constraints.

Head-to-head at 15 m: fast vs. robust

We compared the fast branch (WLS) against the robust branch (refined heatmap) on a 100×100 m scene with a concrete-like wall (f=3.5 GHz, s=15 m, N_{pts}=49, M=9, K_{avg}=5, v=3 m/s, t_h=4 s; R=100). Two fast-branch anchor policies were tested: (A) visibility-aware (LoS prioritized; CV-based per-ray correction on obstructed rays) and (B) naive nearest-anchors (CV on). Results (Table 5.3): *(A)* fast achieves 1.763 m RMSE while robust yields 2.058 m; *(B)* fast degrades to 3.182 m whereas robust remains 2.061 m. The measured coarse-scan time in this setup is $T_{\text{coarse}} \approx 10.1$ min and the refinement adds $T_{\text{refine}} \approx 3.93$ min. **Takeaway:** the fast path wins only with visibility-aware anchor selection (and reliable correction of obstructed rays); choosing anchors solely by distance under NLoS breaks WLS geometry and cedes advantage to the robust branch.

Key quantitative findings

- **Geometry (E4).** Target $N_{\text{pts}}\approx49$ (s=15 m) and $M\approx9$. Moving from s=20 to 15 m yields a clear RMSE drop at only $\sim+16\%$ extra coarse time; further densification to s=10 m almost doubles time with diminishing gains.
- **Operational budget.** With v=3 m/s and t_h=4 s per point, coarse-scan time is $\approx$ 6.3 min at s=20 m (36 pts) and $\approx$ 7.3 min at s=15 m (49 pts). In the head-to-head run with K_{avg}=5, the measured coarse time was $\approx$ 10.1 min; a 5 m warm-zone refinement adds $\approx$ 3.9 min.
- **Switching rule.** When $N>0.3$ the robust branch becomes preferable unless obstructed rays are reliably corrected; for $H\geq0.4$ and $N<0.3$ WLS is consistently better.
- **Temporal averaging (E5).** Averaging improves RMSE from $K_{\text{avg}}=1 \to 3$ and $3 \to 5$, with an elbow at $K_{\text{avg}}\approx5$ (about 5 s dwell). Beyond this point gains saturate and may revert due to non-stationarity; if time-limited, K_{avg}=3 is a good budget choice.
- **Calibration (E3).** A global RSS_0 bias Δ strongly skews raw WLS (±6 dB can shift RMSE by $\mathcal{O}(10)$ m). Material-aware correction flattens the curve to $\approx 4-5$ m, but large $|\Delta|$ still degrades performance — calibration remains necessary.
- **Frequency/materials (E6).** Material ranking is stable (IRR glass and concrete are the harshest). Frequency increases concrete penalties (e.g., raw RMSE grows from $\sim$ 11.7 m at 2.6 GHz to $\sim$ 18.2 m at 4.9 GHz), while oracle correction restores a $\sim 4-4.5$ m floor across bands.

Practical guidance

Default mission planning for a 100×100 m area:

- **Coarse scan.** Use s=15 m ($N_{\text{pts}}\approx49$), M=9, K_{avg}=5. If battery/time is tight, s=20 m and K_{avg}=3.
- **Anchor policy.** Do *not* use "nearest only" under mixed visibility. Prefer *visibility-aware* selection (LoS anchors first); apply per-ray correction to obstructed links when confidence is high, or drop them otherwise.

- **Switching.** If $H \geq 0.4$ and $N < 0.3$ — fast (WLS). If $N \geq 0.3$ and confidence in correction is sufficient, fast-after-correction is viable; else switch to robust (5 m refinement inside the warm zone).
- **Calibration.** Before running WLS, perform a short local calibration of RSS_0 at $d_0 = 1$ m (50–100 snapshots) to suppress global bias.
- **Reporting.** Compute all ground-plane errors with altitude absorbed into the CI intercept (as in Chapter 5); this keeps metrics consistent across runs.

Limitations and threats to validity

Our evaluation uses a 2D ground-plane geometry with altitude handled via the CI intercept and material-dependent penetration with lognormal shadowing. This yields robust trends but introduces limitations:

- **Scene understanding is imperfect.** In Chapter 5, material-aware correction is an upper bound; real CV labels are noisy/incomplete. The fast branch depends on label confidence; uncertain cases must fall back to the robust branch.
- **2D vs. 3D.** Finite obstacle height and true 3D ranges can open LoS corridors above rooftops and alter the fast/robust balance; our results do not model those effects explicitly.
- **Averaging vs. stationarity.** Gains saturate beyond $K_{\mathrm{avg}} \approx 5$; longer dwells risk drift and non-stationarity, potentially increasing RMSE.
- **Penetration composition.** We assume additive losses in dB across layers; real walls may exhibit saturation/leakage effects that deviate from this model.
- **Band generality.** Conclusions are supported for FR1 (2.6/3.5/4.9 GHz); extrapolation to mmWave requires separate validation.

Future work

Using SRS–CIR for UE Localization

In our laboratory setup we successfully extracted the CIR from uplink SRS of a commercial smartphone. This is important because the CIR reveals the earliest arriving path, which can be used for timing- and angle-based ranging.

The main relation is simple:

$$B = N\,\Delta f, \quad \Delta r \approx \frac{c}{B}.$$

Here B is the occupied SRS bandwidth, Δf the subcarrier spacing, and c the speed of light. These parameters define the distance resolution.

With SRS bandwidths between 20 and 100 MHz, the corresponding resolution is in the 15–3 m range, and with sub-sample interpolation the effective accuracy in LoS can often reach 5–10 m.

Future Direction 1: ToA with a single UAV. The simplest approach is to take the first significant CIR path as the arrival time, calibrate the initial offset, and then combine the ranges collected at several waypoints of the UAV. Even 3-5 waypoints are sufficient to localise the UE using a least squares solver.

Future Direction 2: AoA from SRS. Another possibility is to estimate the angle from which the SRS signal arrives. If the UAV is equipped with MIMO antenna, standard direction-finding methods can be used to measure this angle and then intersect bearings from different positions. AoA and ToA can be combined for more accurate estimation of the location of the UE.

In summary, SRS-CIR opens a clear path to more accurate localization methods that go beyond RSS, and could enable meter-level accuracy in future experiments.

Practical plan. In practice, the approach would require an initial calibration of the reference delay τ_0, using as wide SRS bandwidth as possible. Periodic SRS transmissions can then be averaged to reduce noise. The received channel frequency response is converted into a CIR (with zero-padding to improve resolution), and the earliest path is detected adaptively, followed by sub-sample ToA estimation. When multiple synchronized receivers are available, angle-of-arrival can also be estimated. The performance should finally be validated by analyzing position error distributions and the variability of ToA/AoA under both LoS and NLoS conditions.

Additional directions

- **3D propagation and altitude.** Extend to 3D ranges and finite obstacle heights to quantify altitude effects and LoS recovery above rooftops;
- **Adaptive M and outlier-robust LS.** Online selection of M based on geometry and SNR; robust estimators (Huber/RANSAC) to mitigate residual NLoS.
- **Online calibration (E3).** Lightweight bias tracking for RSS_0 and per-anchor offsets during flight.
- **Flight-path optimization.** Plan waypoints to minimize RMSE under energy/time constraints, using the empirical RMSE–time curves (Figs. 5.6–5.5).
- **Field trials.** Validate the switching policy (H, N) and the E4 operating points in outdoor/indoor-mixed scenarios.
- **Integration with satellite NTN.** Offloading and relay through LEO constellations such as Starlink [36];
- **AI-enhanced spectrum sharing.** Intelligent DRL-based anti-jamming and spectrum management for UAV networks [37, 38];

Code availability

All code, notebooks, and figure generators are available at `amalikov2000/Design-and-Implementation-of-UE-` (tag `v1.0-thesis`).

Bibliography

[1] C. D. Newgard, R. H. Schmicker, J. R. Hedges, J. P. Trickett, D. P. Davis, E. M. Bulger, T. P. Aufderheide, J. P. Minei, J. S. Hata, and et al., "Emergency medical services intervals and survival in trauma: Assessment of the "golden hour" in a north american prospective cohort," *Annals of Emergency Medicine*, vol. 55, no. 3, pp. 235–246.e4, 2010.

[2] 3GPP, *NR; NR and NG-RAN Overall Description (Stage-2)*, TS 38.300.

[3] E. D. Kaplan and C. J. Hegarty, Eds., *Understanding GPS/GNSS: Principles and Applications*, 3rd ed. Artech House, 2017.

[4] M. Giordani and M. Zorzi, "Non-terrestrial networks in the 6g era: Challenges and opportunities," *IEEE Network*, vol. 35, no. 2, pp. 244–251, 2020.

[5] S. Hayat, E. Yanmaz, and R. Muzaffar, "Survey on unmanned aerial vehicle networks for civil applications: A communications viewpoint," *IEEE Communications Surveys & Tutorials*, vol. 18, no. 4, pp. 2624–2661, 2016.

[6] 3GPP, "Study on new radio (nr) to support non-terrestrial networks," 3rd Generation Partnership Project (3GPP), TR 38.811, Sep. 2019.

[7] R. Zekavat and R. M. Buehrer, Eds., *Handbook of Position Location: Theory, Practice, and Advances*, 2nd ed. Wiley–IEEE Press, 2019.

[8] 3GPP, "Study on channel model for frequencies from 0.5 to 100 ghz," 3rd Generation Partnership Project (3GPP), TR 38.901, 2022.

[9] CENTUM Lifeseeker. (2020) Lifeseeker airborne geolocation system. [Online]. Available: https://centum.com/en/products/lifeseeker/

[10] *OAIBox 5G Lab Manual*, OpenAirInterface / OAIBox, 2025, version 27.1.

[11] A. Traspadini, M. Giordani, and M. Zorzi, "Uav/hap-assisted vehicular edge computing in 6g: Where and what to offload?" in *Proc. 2022 Joint European Conference on Networks and Communications & 6G Summit (EuCNC/6G Summit)*. IEEE, 2022.

[12] ——, "Real-time hap-assisted vehicular edge computing for rural areas," *IEEE Wireless Communications Letters*, 2023.

[13] D. Wang, A. Traspadini, M. Giordani, M.-S. Alouini, and M. Zorzi, "On the performance of non-terrestrial networks to support the internet of things," in *Proc. Asilomar Conf. on Signals, Systems, and Computers*, 2022, pp. 881–887.

[14] Y. Wang, M. Giordani, and M. Zorzi, "On the beamforming design of millimeter wave uav networks: Power vs. capacity trade-offs," *Computer Networks*, 2022.

[15] C. Codău *et al.*, "Experimental evaluation of an sdr-based uav localization system," *Sensors*, vol. 24, no. 9, p. 2789, 2024.

[16] Y. Li, W. Nie, W. He, Y. Wang, and X. Yang, "Uav 3d localization system using CSI," in *Proc. IEEE Int. Conf. on Microwave and Millimeter Wave Technology (ICMMT)*, May 2021, pp. 1–6.

[17] M. Polese, M. Giordani, and M. Zorzi, "3gpp nr: the standard for 5g cellular networks," in *5G Italy White eBook: from Research to Market*. CNIT, 2018.

[18] S. Sesia, I. Toufik, and M. Baker, *LTE – The UMTS Long Term Evolution: From Theory to Practice*, 2nd ed. Wiley, 2011.

[19] N. Modina, R. Ferrari, and M. Magarini, "A machine learning-based design of prach receiver in 5g," in *Proc. RACT-5G-IoT*, 2020.

[20] 3GPP, *NR; Physical Channels and Modulation*, TS 38.211, 2023, release 17.

[21] R. Schmidt, "Multiple emitter location and signal parameter estimation," *IEEE Transactions on Antennas and Propagation*, vol. 34, no. 3, pp. 276–280, 1986.

[22] R. Roy and T. Kailath, "Esprit—estimation of signal parameters via rotational invariance techniques," *IEEE Transactions on Acoustics, Speech, and Signal Processing*, vol. 37, no. 7, pp. 984–995, 1989.

[23] A.-J. van der Veen, M. Vanderveen, and A. Paulraj, "Joint angle and delay estimation using shift-invariance techniques," *IEEE Transactions on Signal Processing*, vol. 46, no. 2, pp. 405–418, 1998.

[24] M. Rawat, M. Giordani, B. Lall, A. Chaoub, and M. Zorzi, "On the optimal beamwidth of UAV-assisted networks operating at millimeter waves," in *Proc. IEEE Wireless Communications and Networking Conference Workshops (WCNC WKSHPS)*. IEEE, 2023.

[25] Y. Li, B. Mukhopadhyay, and M.-S. Alouini, "Experimental validation of cooperative RSS-based localization with unknown transmit power, path loss exponent, and precise anchor location," 2024.

[26] A. Traspadini, M. Giordani, G. Giambene, T. De Cola, and M. Zorzi, "On the energy consumption of UAV edge computing in non-terrestrial networks," in *Proc. Asilomar Conference on Signals, Systems, and Computers*. IEEE, 2023.

[27] A. Alnoman, A. S. Khwaja, A. Anpalagan, and I. Woungang, "Emerging ai and 6g-based user localization technologies for emergencies and disasters," *IEEE Access*, vol. 12, pp. 197 877–197 906, 2024.

[28] X. Li, "RSS-based location estimation with unknown path-loss model," *IEEE Transactions on Wireless Communications*, vol. 5, no. 12, pp. 3626–3633, Dec. 2006.

[29] DroneBase. (2025) X4-1000 pro rtk technical specifications. [Online]. Available: https://dronebase.it/en/x4-1000-pro-rtk/

[30] N. Patwari, J. N. Ash, S. Kyperountas, A. O. Hero, R. L. Moses, and N. S. Correal, "Locating the nodes: Cooperative localization in wireless sensor networks," *IEEE Signal Processing Magazine*, vol. 22, no. 4, pp. 54–69, 2005.

[31] 3GPP, *NR; Medium Access Control (MAC) Protocol Specification*, TS 38.321.

[32] J. Bultmann *et al.*, "Real-time multi-modal semantic fusion on unmanned aerial vehicles," 2021.

[33] T. Nguyen *et al.*, "Mavnet: An effective semantic segmentation micro-network for MAV-based tasks," 2019.

[34] S. Sun, T. S. Rappaport, S. Rangan, T. A. Thomas, and A. Ghosh, "Path loss models for 5g urban micro- and macro-cellular scenarios," in *Proc. IEEE VTC-Fall*, 2016.

[35] G. R. MacCartney and T. S. Rappaport, "Rural macrocell path loss models for 5g wireless communications," in *Proc. IEEE ICC*, 2017.

[36] A. Bonora, A. Traspadini, M. Giordani, and M. Zorzi, "Performance evaluation of satellite-based data offloading on starlink constellations," in *Proc. IEEE Wireless Communications and Networking Conference (WCNC)*. IEEE, 2025.

[37] R. Ding, Z. Zeng, H. Quan, F. Zhou, M. Giordani, Q. Wu, and M. Zorzi, "An intelligent game theoretic drl anti-jamming framework for spectrum sharing uav networks," in *Proc. IEEE Global Communications Conference (GLOBECOM)*, 2025, submitted.

[38] R. Ding, F. Zhou, M. Giordani, Q. Wu, and M. Zorzi, "Towards 6g: Spectrum management in low-altitude aerial information networks," *IEEE Wireless Communications Magazine*, 2025, submitted.

Acknowledgments

I am deeply grateful to Prof. Marco Giordani for his priceless guidance throughout this project and for conceiving the core idea of this research, through which I gained a extensive amount of practical experience.

My warmest thanks go to my family for their constant support over countless video calls, always reminding me that things would work out; and to my best friends, Dasha and Grisha, for their steady mental support.

I am also thankful to my wonderful neighbors—especially Delia and Angelina—who refused to let me stay locked up for days and made sure I stepped out and enjoyed life.

To my "second family" in Padov-ha: thank you for standing by me throughout these years of study and for making me feel at home from the very beginning.

I owe special thanks to my colleague and dear friend Dasha, who helped me to find my place at university, get used to the city, and guided me through courses over the years—without her, I would not have completed this degree.

I am grateful to my friends Alina, Katherine, and Maxim for being there during the hardest moments of emigration.

Finally, my deepest thanks to Antonio for his patience and support over the last two years, enduring all my mental breakdowns with kindness and strength.